Diffusion in
Zr-based glass forming melts

Dissertation

zur Erlangung des akademischen Grades
Doktor der Ingenieurwissenschaften
(Dr.-Ing.)
der Technischen Fakultät
der Christian-Albrechts-Universität zu Kiel

vorgelegt von
Sri Wahyuni Basuki

Kiel 2015

1. Gutachter: Prof. Dr. Klaus Rätzke

2. Gutachter: Prof. Dr. Jeffrey McCord

Datum der mündlichen Prüfung: 08. 04. 2015

Kurzfassung

In einfachen metallischen Schmelzen, die sich im Gleichgewicht befinden, werden keine dynamische Asymetrie und daher auch keine großen Unterschiede in den Diffusivitäten der einzelnen Bestandteile erwartet. In vorherigen Untersuchungen von Pb-basierten glasbildenen Mehrkomponenten-Schmelzen, gingen die Diffusivitäten aller Komponenten in eine Temperaturabhängigkeit über und die größte Komponente, Pb, folgte der Stokes-Einstein (SE)-Relation in allen Temperaturbereichen von stabiler Schmelze bis zur Glasübergangstemperatur. Es ist sehr interessant zu überprüfen, ob diese Ergebnisse genereller Natur sind und auch für andere Klassen von metallischen Glasbildnern, wie z.B. Zr-basierte Glasbildner zutreffen. Daher werden gleichzeitige Radiotracer Diffusions Experimente von ^{57}Co und ^{95}Zr in der Schmelze des Multikompentensystems $Zr_{46.75}Ti_{8.25}Cu_{7.5}Ni_{10}Be_{27.5}$ (Vitreloy 4) und der einfacheren Systeme $Zr_{64}Ni_{36}$, $Zr_{36}Ni_{64}$ und $Zr_{60}Ni_{25}Al_{15}$ oberhalb ihrer jeweiligen Schmelztemperaturen, T_l, durchgeführt. Durch diese Messungen werden die Effekte der Komplexität der Komponenten auf die atomare Diffusion in der Schmelze verstanden werden können. Zusätzlich wird erwartet, dass durch die Untersuchungen der einfacheren Systeme die atomare Diffusion in Zr-bsaierten Mehrkomponentensystemen sowie der Einfluß der Packungsdichte und der chemischen kurzreichweitigen Ordnung (checmical short range order, *CSRO*) auf die atomare Diffusion erklärt werden können. Die Resultate der Mehrkomponenten-Schmelze Vit. 4 zeigen, dass die Diffusivität von Zr sich von der Diffusivität der kleineren Komponenten um einen Faktor 4 an ihrer T_l unterscheidet, obwahl sie der SE-Relation folgt. Auf der anderen Seite ist das Verhältnis aus den Diffusivitäten von *Co* und *Zr* in den eifachen Zr-basierten Systemen gleich dem Verhältnis der Diffusivitäten in einfachen metallischen und Pb-basierten Schmelzen, obwohl es von $Zr_{64}Ni_{36}$ über $Zr_{60}Ni_{25}Al_{15}$ zu $Zr_{36}Ni_{64}$ jeweils ansteigt. Diese Ergebnisse suggerieren, dass in dem Mehrkomponentensystem Vit. 4 Zr-Atome ein Energielandschafts-kontrolliertes Regime betreten und sich zumindest 150 K über ihrer T_l wie Festkörper verhalten. Außerdem zeigen die Ergebnisse die Effekte der Packungsdichte und CSRO auf die atomare Diffusion, obwohl die die Diffusion in dem einfacheren System aus Zr-basierten Schmelzen einfachen metallischen Schmelzen sehr ähnlich ist.

Abstract

In simple metallic melts, which are supposed to be in equilibrium, dynamic asymmetry and thus large differences in diffusivities of the constituents are not expected. For instance, on the previous investigation in multicomponent Pd-based glass forming melts, diffusivities of all components merge into one single temperature dependence, and the majority component Pd obeys Stokes-Einstein (SE) relation in the whole temperature range; from the stable melt down to the glass transition temperature. It is interesting to check whether these results are generally accepted also for another class of metallic glass formers, e.g. Zr-based glass formers. Therefore, simultaneous radiotracer diffusion experiments of ^{57}Co and ^{95}Zr in the melt of multicomponent system, $Zr_{46.75}Ti_{8.25}Cu_{7.5}Ni_{10}Be_{27.5}$ (Vitreloy 4), and of the simpler systems, $Zr_{64}Ni_{36}$, $Zr_{36}Ni_{64}$ and $Zr_{60}Ni_{25}Al_{15}$ above their respective liquidus temperature, T_l, are performed. From these experiments, the effects of component complexity on the atomic diffusion in the melt can be understood. Additionally, from the experimental results of the simpler systems, the atomic diffusion in the multicomponent Zr-based systems, as well as the effects of packing density and chemical short range order (CSRO) on the atomic diffusion, can also be explained. The results in multicomponent Vit. 4 melt show that Zr diffusivity differs significantly from the diffusivities of the smaller components by a factor of 4 at its T_l, although it obeys SE relation. On the other hand, the Co and Zr diffusivities ratio in the melt of the simpler Zr-based systems is the same as the component diffusivities ratio in simple metallic and Pd-based melts, although it increases sequentially from $Zr_{64}Ni_{36}$ to $Zr_{60}Ni_{25}Al_{15}$ and $Zr_{36}Ni_{64}$. These results suggest that in multicomponent Vit.4, Zr atoms enter energy-landscape-controlled regime and behave solid-like already at least $150\ K$ above its T_l. Additionally, although the diffusion in the simpler system of Zr-based melts is similar to the simple metallic melts, the results show the effects of packing density and CSRO on the atomic diffusion.

Contents

List of figures

Chapter 1 Introduction

Metallic glasses, especially bulk metallic glasses (BMGs), have become very interesting engineering materials since the first time they were invented in about 30 years ago [1-2]. They are among the strongest engineering materials, and some of them are also tough. They can also be formed into the desired shape by, e.g. compression, injection moulding, extrusion etc. just like plastics. Because of these excellent properties, BMGs have been used in many applications such as micro-electronics sensors, electronic casings, medical implants and devices, jewellery, etc. [2-6]. However, the material cost of BMGs makes them unfavourable for industrial use. BMGs comprise materials that cost around $100/kg, while common steels average about $1/kg [2]. Therefore, the scientific communities still continuously and actively conduct research to find next-generation of BMGs with using low cost elements for large-scale industrial use. And understanding the glass formation in BMGs can be the key of this success.

Not like in traditional oxide glasses or amorphous semiconductors, metallic glass formers have no strong directional covalent bond. The bond in metallic glass formers is attributed to the isotropic character of the metallic bond. This is why forming a glass from metallic glass formers is a challenging work. Conventional metallic glass formers, which are mostly binary systems, must be rapidly quenched with rates up to $10^{10}\ K\ s^{-1}$ for vitrification. They have poor glass forming ability (GFA) and can only be produced in a very thin sheet of about few μm. Multicomponent has long been known as one of some prerequisites for good GFA and can be used to produce bulk metallic glasses with critical thickness up to several cm. It is because when multiple chemically different atoms are introduced, the crystalline structure becomes very complex, and atoms should travel very long distance in order to arrange themselves to form crystalline structure. This arrangement of many variety of atoms with different sizes is well known as "confusion principle".

As bulk metallic glasses are produced by rapid cooling of the melt and the glass forming ability is determined by how fast the arrangement of the constituted atoms in the melt, information about diffusion of atoms in the melt becomes very important. Recently, atomic diffusion in melts has been extensively studied experimentally [7-10] and using computer simulation [11-13] to study the solidification, and hence glass formation behaviour. In an ideal melt at high temperature, diffusion proceeds via uncorrelated binary collisions between the atoms, and dynamic asymmetry in this regime should be absent as reflected in the Stokes-Einstein relation. Therefore, component diffusivities should only differ by factor being proportional to the radii or the square root of the masses, i.e. less than a factor of two. Thus, component diffusion decoupling will only be used in terms of diffusivities difference of more than a factor of two. As temperature decreases and the liquid enters the supercooled liquid regime, the movement of the atoms becomes correlated and dynamic asymmetry sets in. The dynamic asymmetry becomes very strong in glassy state where the atoms have to overcome high activation barriers by local hopping and diffusivities of the larger and smaller atoms can differ by many orders of magnitude. This has been frequently interpreted as the evidence of dynamic heterogeneity.

In energy landscape point of view, at low temperatures, atoms sample deeper energy landscape valley and behave solid-like. While as the temperature increases, the atoms mobility will be less and less controlled by the energy landscape. At some point they sample almost the entire energy landscape with shallow minima and move almost freely, thus behave liquid-like. Apart from this, it has been reported that diffusivities in highly dense metallic melts are affected by size effects such as packing density [14-15]. Moreover, it has also been reported that the present of chemical short range order (CSRO) in the structure of the melts may influence the size effects and the interaction among atoms [15], and thus it influence also the diffusivities [16].

Mode coupling theory (MCT) has long been widely used to predict the slowing down of the atomic dynamics at critical temperature (T_c). The previous investigation in multicomponent Pd-based alloy [17] was in good accordance with the onset of liquid-like motion at T_c of MCT. In this glass forming system, diffusivities of all components merge into one single temperature dependence above T_c. Below T_c, the diffusivity of majority component Pd decouples largely from the smaller components.

Although Pd-based systems have been known to have the best GFA [2, 18], Pd is a very expensive element and therefore unfavourable for industrial application. Therefore the investigation is extended to Zr-based glass formers which are more realistic being used in industry. Indeed, Zr-based BMG family has been commercialized and used for electronic casings, e.g. Vitreloy family by Liquidmetal® Technologies, although Vitreloy family still contains beryllium which is toxic.

In the present work, there are two goals to be achieved. The first goal is we want to see whether the result in multicomponent Pd-based systems can be generally applicable also in multicomponent Zr-based systems. And the second is to understand the diffusion processes in multicomponent Zr-based melts, $Zr_{46.75}Ti_{8.25}Cu_{7.5}Ni_{10}Be_{27.5}$ with commercial name Vitreloy 4 (Vit. 4). In order to accomplish those goals, this work is divided in to two parts. Part I is simultaneous radiotracer diffusion measurement of ^{95}Zr and ^{57}Co in multicomponent Vit. 4 above the liquidus temperature, T_l. ^{57}Co is used as a substitute for Ni which represents the smaller components. Part II will deal with the understanding of the diffusion process of Zr and Ni in the multicomponent Zr-based glass forming melts by measuring ^{95}Zr and ^{57}Co diffusivities in the melt of simpler Zr-based systems, i.e. $Zr_{64}Ni_{36}$, $Zr_{36}Ni_{64}$ and $Zr_{60}Ni_{25}Al_{15}$. From the results of Part II, it is expected that the behaviour of Zr and Ni diffusivities in multicomponent Vit. 4 in terms of energy landscape point of view can be explained. Additionally, the effects of the size effects and the presence of CSRO in the structure on the atomic diffusion are also expected to be explained.

The content of this dissertation is divided into five chapters. Chapter I is this chapter, introduces briefly the background and the goals of the current investigation, as well as the structure of this dissertation. Chapter II deals with the basic theory relevant to the present investigation, such as the general properties of metallic melts, theories which can explain the dynamics of atoms and an overview of the current investigation. In Chapter III, the experimental techniques specifically on the radiotracer diffusion measurement will be explained. The results of the experiments, as well as the discussion, are given in Chapter IV. And finally, the conclusion of the current investigation, and the outlook for the future investigation, are given in Chapter V.

Chapter 2 Theory

In this Chapter, the general description of melts is given according to the existing theories. Later, the structure of the melts, and the principle of how to measure it, are also given. After that, the atomic transport properties in the melt are also given. In the end of this chapter, general description about the present investigation which includes the aims, the properties of the alloys being used and the basic principle of diffusion measurements relevant to the present investigation are explained.

2.1 Metallic glass forming melts

Melts are normally thermodynamically in equilibrium, which means there is no driving force to minimize their energy, because their Gibbs free energy is already minimal. Melts have maximum entropy and enthalpy. When a metallic melt at high temperature is cooled down with so high cooling rate that the crystallization is avoided, the melt will transform into supercooled melt and finally a glass. These states are metastable states because the Gibbs free energy is still higher than for the crystalline state. When melts transform into suppercooled melts and glasses, it is followed by continuous decrease of enthalpy, entropy and volume. The slope over temperature, of enthalpy, entropy and volume, decreases with temperature and changes into lower slope at the glass transition temperature, T_g. A glass which is produced by lower cooling rate has lower T_g than a glass which is produced by higher cooling rate, as indicated in Figure 2-1. On the other hand, when the cooling rate is so low that it allows nucleation and crystal growth, a crystal is formed. It is followed by an abrupt decrease of the enthalpy, entropy and also volume, which normally occurs at the liquidus temperature.

Describing the properties of metallic melts is a great challenge. Their structure is random like gases, but their interatomic distance is much closer than that

of gases and influenced by many body interaction. Therefore, they cannot be treated as simple as gases. Structures of melts are also amorphous like glasses, but their dynamics is not as strongly correlated as that of glasses. Describing the properties of glasses is already a challenge due to the lack of long range order, and the properties cannot be described in simple way such as in crystals.

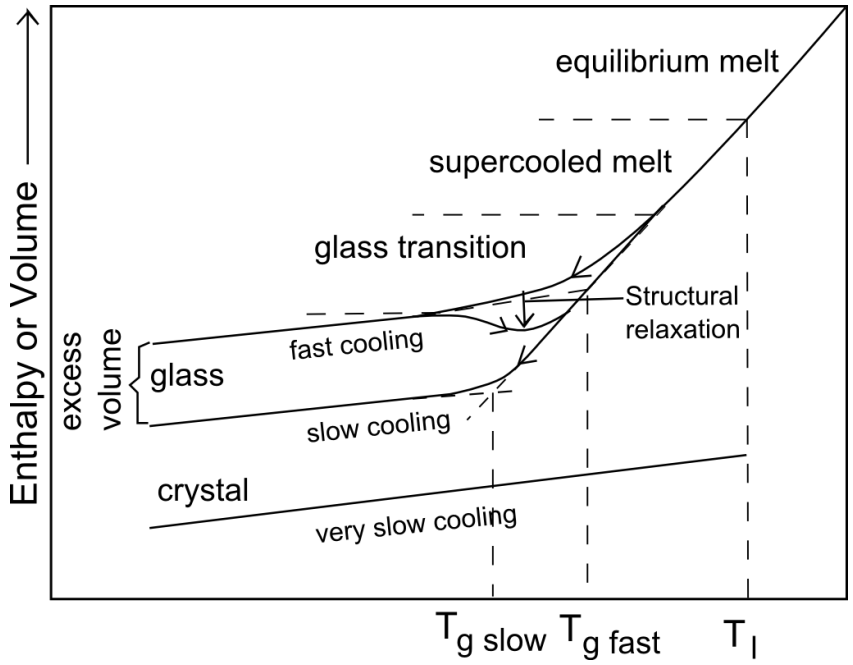

Figure 2-1 Illustration of glasses and crystals formation and the corresponding thermodynamics properties (adapted from ref. [19-20])

Studies about atomic diffusions in liquid have been started at least as early as in 1827 when Robert Brown (1773-1858) observed the phenomenon of irregular motion of small particles suspended in a liquid, this phenomenon is well known as Brownian motion [21]. There was not much progress made in understanding the Brownian motion until Einstein in 1905 [22], and Sutherland in the same year [23], provided mathematical solution of Brownian motion which is nowadays known as Stokes-Einstein relation which relates atomic diffusion and macroscopic viscosity. However the development of atomic transport theory in dense fluid was still not so much done after that, until the success of Cohen and Turnbull in 1961 in quantifying

the concept of free volume theory which relates the viscosity to its volume. This theory has been used for long time to discuss atomic transport in many materials. According to the free volume theory, an atom can diffuse to its next nearest neighbour sites when a free volume of about 80% of its atomic volume in the next nearest neighbour is available. However, in metallic liquids, it is only 10% for metallic liquids [24]. It seems that this theory is not enough to explain the atomic transport in metallic glass formers. Additionally, molecular dynamic simulations [25] and some experiments [26-27] have shown that in metallic glasses, atoms move in a more collective and chain-like diffusive process which involves tens of atoms.

As bulk metallic glasses (BMGs) are advanced engineering materials with excellent functional properties but are very expensive, there are a lot of attempts being done to find new classes of BMG which are more favourable for industrial application. In addition, as bulk metallic glasses are produced by rapid cooling of the melt, and the glass forming ability is determined by how fast the arrangement of constituted atoms in the melt, information about diffusion of atoms in the melt, as well as the crossover of atomic motions in solid to melt regime, becomes very important. Nowadays, there are a lot of theories which are also developed in order to explain the crossover of solid- to liquid-like motion of metallic glass formers. Two theories which are used for long time to test the onset of liquid-like motion are Stokes-Einstein relation and mode coupling theory. Some simulations [11, 13] and experiments [28] have proven the validity of these theories in predicting the onset of liquid-like motion in some metallic glass formers, which is at the critical temperature, T_c, of mode coupling theory. However, some simulations [11, 15, 29] and experiment [30] in hard-sphere and simple binary systems have also shown the violation of Stokes-Einstein relation which extends even in the melt of some metallic glass formers. According to our knowledge so far, there is no experiment, which has shown such violations, has been done in bulk (or multicomponent) metallic glass former melts. Therefore, the present investigation will be the first experimental evidence

which shows that Stokes-Einstein relation and mode coupling theory cannot be used to generalize the transport properties of metallic melts.

In order to give the reader a little background about the ideal transport properties of metallic melts, in the following sections an overview about the general properties of the metallic melts in the view of different theories is given.

2.1.1 Potential energy landscape

Potential energy landscape is often used as a convenient way to describe the complex phenomenology of glass forming systems [31-32]. Energy landscape is generally described as potential energy as a function of N-body systems, $E_p(r_1,...,r_N)$, where the vectors r_i corresponds to position, orientation and vibration coordinates [31]. It is a set of topographic of energy potential consisting of many valleys and saddle points with respect to all configurational coordinates of particles as seen in Figure 2-2. The shape of energy landscape is determined by the packing density, and the number of minima in the landscape depends significantly on the chemical nature of the substance being considered. While the temperature corresponds to the way in which the landscape is sampled.

From the point of view of energy landscape, at high temperature as the system possesses sufficient kinetic energy to sample entire energy landscape, and the energy minima of the sampled landscape are shallow, the system exhibits a temperature-independent activation energy. At this condition, particles diffuse almost freely, resembling liquid-like motion. As the temperature decreases, and as the activation energy increases, the particles sample deeper minima of the landscape energy. In this condition the dynamics become "landscape-influenced" and behave solid-like.

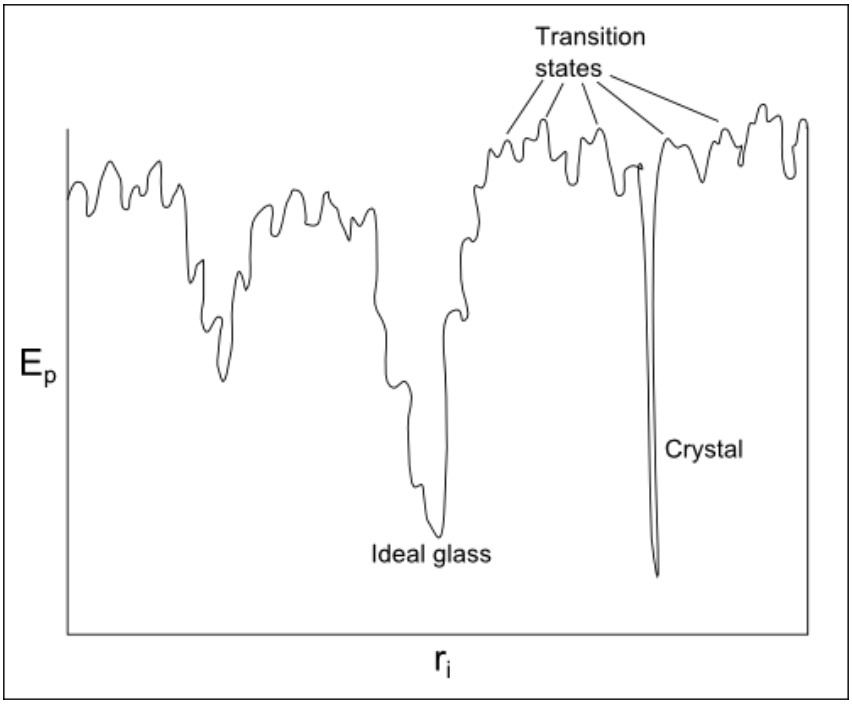

Figure 2-2 Illustration of an energy landscape, energy potential, E_p, as a function of all configurational coordinates, r_i, (adapted from ref. [31])

2.1.2 Mode coupling theory

Mode coupling theory (MCT) predicts the transition from ergodic phase of liquid to completely non-ergodic phase of glass at critical temperature T_c [33]. The dynamics property of a system according to MCT can be understood in terms of density correlation function $\phi(q,t)$ which measures the correlation of a system density at one time with the density of another time.

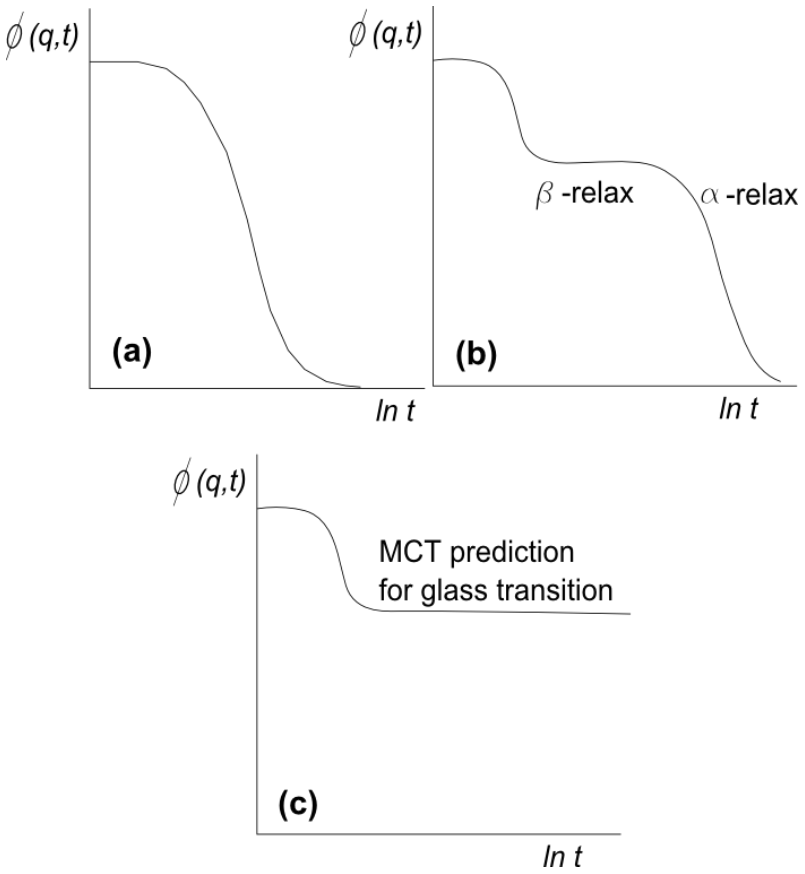

Figure 2-3 Types of $\phi(q,t)$ decay at different temperature regimes: (a) at temperatures above T_l (liquid), (b) at temperatures $T_c < T < T_l$ (super-cooled) and (c) at temperatures below T_c (glass) (adapted from ref [33])

In the point of view of MCT, in the melt regime, the density of the system immediately becomes uncorrelated, and the correlation function $\phi(q,t)$ decays like a single-exponential function as sees in Figure 2-3a. Although for a very short time, $\phi(q,t)$ decays due to collision events involving local particle motion and the particle density is still highly correlated. As the temperature is lowered and the system entered super-cooled liquid regimes (see Figure 2-3b), at intermediate times, particles are trapped in cages formed by neighbourhood particles which is called as β-relaxation. After long time, particles enter the α-relaxation regime and $\phi(q,t)$ decays to zero with decay function may fit to stretched exponential function [33]. When the temperature is further lowered and approaching the critical temperature T_c, the relaxation time becomes very large and the $\phi(q,t)$ does not decay as $t \to \infty$, as seen

in Figure 2-3c. At this point, the system transforms into a glass, and the relaxation time τ scales as [33-34]

$$\tau(q,T) \approx A(T - T_c)^{-\gamma} \qquad (2\text{-}1)$$

and diverges as a power law with a universal exponent γ. Relaxation time τ corresponds to all transport coefficients such as diffusivity D and viscosity η.

In other words, MCT predicts the transition from liquid-like motion to solid-like motion at T_c which is often found to be around 20-30 % above T_g. Although it is well known that there is deviation in MCT prediction for the glass transition temperature, T_g, MCT prediction is remarkably true at high temperatures in the supercooled and liquid regime, i.e. above T_c.

2.1.3 Stokes-Einstein relation

Stokes-Einstein (SE) relation was first derived by Sutherland [23] in 1905 to solve the Brownian motion of particles [21]. Independently, but with identical argument as Sutherland had, Einstein published his Ph.D. work in 1905 stated that the diffusivity D of a suspended substance depends only on the absolute temperature T and a friction coefficient which is proportional to the viscosity η and the size r of the suspended particles [22]. It is written as

$$D = \frac{k_B T}{6\pi\eta r} \qquad (2\text{-}2)$$

SE relation has long been used to understand the transport properties in metallic glass formers, usually by comparing the measured diffusivity with the diffusivity converted from the measured viscosity using SE relation. As mentioned

above, in the equilibrium melt of a simple metal, atoms move via uncorrelated binary collision. Therefore, they should move almost equally and SE relation should hold reasonably well for all constituents of the melt [17, 35-36] and above the critical temperature T_c of mode coupling theory. In supercooled and glassy regime which is below T_c, however, SE relation holds only for the majority constituent, and does not hold for the smaller constituents [17]. The breakdown of SE relation at T_c is expected as evidence of the dynamic heterogeneity.

2.1.4 Atomic connectivity network

The theory of atomic connectivity network or local topological network in liquid structure was first proposed by Egami in 1980 [37]. In atomic connectivity networks, the local atomic structure is described from a general topological approach to understand the properties of metallic glasses. In the melt at high temperatures, atomic bonds are broken and formed at the same rate as the vibration of an atom leading to the local topological fluctuation changes with time and temperature. Once the structure is defined as the topology of the nearest neighbours, diffusion and any structural change can also be described in terms of the change of the atomic connectivity or local topological network.

Using the approach of local atomic connectivity, Egami introduced elementary excitation which exist in liquid and is different from phonons. He studied it using computer simulation [38]. Within this approach, he also introduced a new characteristic temperature, called crossover temperature, T_A. It is the temperature below which the Maxwell relaxation time, τ_M, deviates from the local atomic connectivity life time, τ_{LC}.

Maxwell relaxation time determines the time scale of liquid dynamic, written as

$$\tau_M = \frac{\eta}{G_\infty} \qquad (2\text{-}3)$$

with G_∞ is the high-frequency shear modulus. This relaxation time is also known as macroscopic relaxation time. If the time scale of the observation is shorter than τ_M, the system behaves like a solid. And when it is longer, the system behaves like a liquid. The lifetime of local atomic connectivity, τ_{LC}, is defined as the time for an atom to lose or gain one nearest neighbour, and it measures the microscopic quantities of the system [38]. Both, τ_{LC} and τ_M, show Arrhenius-like behaviour at high temperature, but deviate from each other as the temperature is lowered below T_A.

The dynamical matrix of a liquid varies as fast as, or faster than phonons. In other words, phonons in liquid are short lived and cannot be used as the basis to explain macroscopic properties of liquid, such as viscosity [24]. However, these properties can be explained by the other elementary excitation in liquid, which is the local configurational excitation (LCE) which life time refers to τ_{LC}. As the temperature is lowered below the crossover temperature, T_A, atoms are able to communicate with the neighbours through atomic vibration and the macroscopic properties can be explained by phonons. This means T_A is related to the crossover of phonons into LCEs. In other words, above T_A, the lifetime of the local atomic configuration is so short that the local atomic connectivity changes before atoms communicate with the neighbours through atomic vibration, and LCEs are independent from each other. Below T_A, LCEs create dynamic long-range stress fields around them, and with these fields, LCEs can interact with each other. This is the reason behind the deviation of τ_{LC} from τ_M below T_A.

2.2 Structure of melts

The structure of melts are random but not as completely random as the structure of gases. Although the long range order is absent in the melts, the short or medium order is still maintained. And the best way to describe the structure of melts is using pair distribution function $g(r)$ as depicted in Figure 2-4. $g(r)$ is the distribution of the

distances between pairs of atoms which are averaged over time and over all atoms. It can be determined from scattering experiments; either by electrons, X-rays, or neutrons. It is obtained from fourier transform of the structure factor, $S(q)$. From $g(r)$, radial distribution function (RDF) can be calculated by $4\pi r^2 n_0 g(r)$, where n_0 is the number density. The first coordination number can be calculated from the area under the first peak of RDF, and it is the number of nearest neighbours, which is often an important parameter when describing the short range order structure of a melt.

In order to completely describe the structure, several partial pair distribution functions are required. The number of the partial pair distribution functions depends on the total combination number of the system components. For instance in binary systems of component 1 and 2, three partial pair distribution functions $g_{11}(r)$, $g_{12}(r)$ and $g_{22}(r)$ are required. These three partial pair distribution functions are obtained from three independent measurement of partial structure factors $S_{11}(q)$, $S_{12}(q)$ and $S_{22}(q)$. For ternary systems, 6 partial pair distribution functions from 6 independent measurements of partial structure factors are required to complete the description of their structure. As the measurement of one partial structure factor is not that easy, it is very rare to find the experimental data of systems with three or more components. In most ternary systems, their structures are mostly described using molecular dynamic (MD) simulation. And in more complex systems, such as in five component system, the MD simulation is not even available.

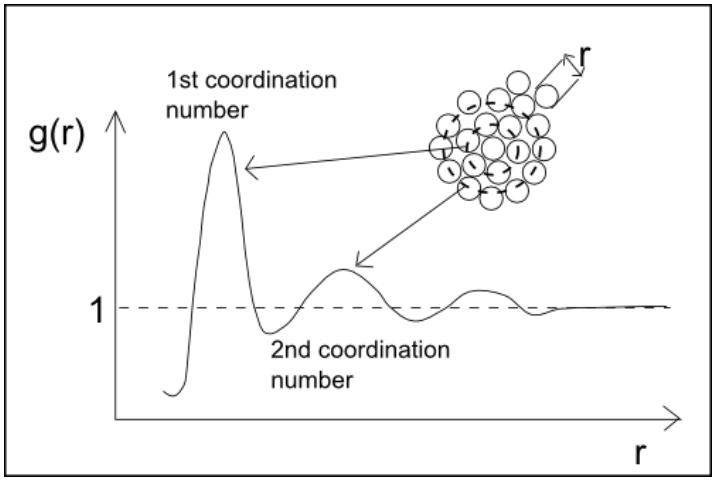

Figure 2-4 A typical curve of pair distribution function $g(r)$ (adapted from Ref. [39])

The short range order in melts originates from the chemical nature of the constituents and the need to achieve as compact as possible geometrical packing. The pronounce effect of the first leads to the pronounce chemical short range order (CSRO) which can be visualized through the pre-peak of the first peak in the structure factor [15-16] or pair distribution function [40]. And the arrangement of the first neighbour atoms due to geometrical origin refers to topological short range order [41].

2.3 Transport properties

2.3.1 Diffusion

Diffusion process is defined as a movement of marked particles through a matrix as a result of thermal vibrations and expansion. The experimental studies of diffusion process in liquid was first initiated by Thomas Graham who did quantitative study of diffusion of salts in water [19]. The work of Graham was later described mathematically by Adolf Eugen Fick in 1855 [19]. Fick was the first who introduced the concept of diffusion coefficient and measured it for diffusion of salts in water. His work was later known as Fick's laws [19].

Fick's first law is written mathematically as

$$J = -D\frac{dC}{dx} \qquad (2\text{-}4)$$

which relates diffusion flux, J, and the concentration gradient of diffusing particles with opposite direction to each other. The factor D in Eq. (2-4) denotes diffusion coefficient (or diffusivity) of the species being considered. Fick's second law which is written as

$$\frac{\partial C}{\partial t} = D\frac{\partial^2 C}{\partial x^2} \qquad (2\text{-}5)$$

predicts how diffusion causes concentration change with time, t. The two Fick's laws are used as the basic principle for direct methods of diffusion measurement, such as radiotracer method used in the present investigation (see section 2.4.3). Other diffusion experiment methods which are not based on Fick's laws refer to indirect methods, e.g. in quasi-elastic neutron scattering (QNS) as described in section 2.4.3.

In solid state, the temperature dependent diffusivity of a system normally follows Arrhenius law,

$$D = D_0 \exp\left(-\frac{E_a}{k_B T}\right) \qquad (2\text{-}6)$$

with D_0 is the pre-exponential factor and E_a is the activation energy of diffusion. In other words, atoms need to overcome a certain amount of energy barrier in order to diffuse to the next neighbours with rate proportional to the vibration frequencies of the atoms. And according to harmonic oscillator theory, the vibration frequencies are inversely proportional to the square-root of atomic masses. This implicitly shows that the diffusivity of an atom in solid is also inversely proportional to the square-root of its mass,

$$D \propto \frac{1}{\sqrt{m}} \qquad (2\text{-}7)$$

Strangely, Eq. (2-7) seems to hold also in the melt. Atoms in the melt can diffuse to the next neighbors without the influence of activation energy. And as diffusion is a result of thermal vibrations and expansion, one may adopt the kinetic theory of gases and estimate to calculate the diffusivity as,

$$D = \frac{1}{3}\bar{v}\lambda \qquad (2\text{-}8)$$

with λ is the mean free path and $\bar{v}$ is the mean velocity [42] described as

$$\bar{v} = \sqrt{8k_B T / \pi m} \qquad (2\text{-}9)$$

with m is the mass of the particles, k_B is Boltzmann constant and T is the temperature. And here Eq. (2-9) implicitly also tells Eq. (2-7), which predicts diffusion of atoms in simple binary metallic melts.

Furthermore, in simple binary metallic melts, which are expected to be in equilibrium, atoms move via uncorrelated binary collision. Therefore, one should expect that dynamics asymmetry, as reflected from different diffusivities of the constituents, is absent. Thus, Stokes-Einstein relation, explained in Section 2.1.3, should be valid and D is also inversely proportional to the atomic radii.

$$D \propto \frac{1}{r} \qquad (2\text{-}10)$$

Therefore, both Eq. (2-7) and Eq. (2-10) can be used to describe diffusion of atoms in simple metallic melts which originates from size effects (atomic radius and mass). In other words, if one compares the diffusivities of the components in simple metallic melts, one would expect the diffusivities difference to be in the range of the

mass or radius difference of the components being considered, which is normally less than a factor of two. In this case, it is not categorized as component diffusion decoupling. And indeed it has been reported in Pd-based glass former melts that there is no component diffusion decoupling between the larger component Pd and the smaller components above T_c of mode coupling theory (MCT) [17]. This report is in accord to the prediction of MCT about the onset of liquid-like motion at T_c. On the other hand, component diffusion decoupling between the larger and the smaller components have been generally known in super-cooled and glassy regimes of metallic glass formers, which is predicted by MCT to be at temperatures below T_c . In these regimes, the movement of atoms becomes highly correlated and atoms have to overcome high activation barrier in order to move. Therefore, the diffusivities of the larger and smaller components can differ by many orders of magnitude (component diffusion decoupling).

2.3.2 Viscosity

The same as diffusivity, viscosity is also an important parameter to describe the properties of atoms in a system. Viscosity of a melt is a measure of its resistance to gradual shear deformation. Similar to diffusivity, viscosity is temperature dependent. And according to how viscosity depends on the temperature, glasses can be divided into two categories; one is strong glasses and the other is fragile glasses. In strong glasses, viscosity η can be fitted with Arrhenius law

$$\eta = \eta_0 \exp\left(\frac{E_a}{k_B T}\right) \qquad (2\text{-}11)$$

with E_a is the activation energy and k_B is Boltzmann's constant. Strong glasses normally have strong covalent bonds such as Silica (SiO_2) glasses. On the other hand, the viscosity of fragile glasses, particularly when they are heated, falls abruptly above T_g , as if the system architecture is really fragile and collapses rapidly. Fragile glasses

deviate from Arrhenius behaviour and follow Vogel-Fulcher-Tammann (VFT) temperature dependent viscosity.

$$\eta = \eta_0 \exp\left(\frac{A}{T - T_0}\right) \qquad (2\text{-}12)$$

Most systems without non-directional bonds such as in metallic glass formers are found to be fragile [34].

As mentioned in section 2.1.3, in most simple metallic melts, viscosity is related to diffusivity by Stokes-Einstein relation. However, different from diffusivities which have an implicit structural origin, viscosity provides more general information about the statistics of dynamics [17].

2.4 The present investigation

Before we go into detail about the present investigation it is better to inform the reader about two different terms of decoupling which are explicitly described in section 2.3.1 and 2.3.2, and are the main study of this investigation. The first decoupling is the component diffusion decoupling which is diffusivities difference between one component to the others in an alloy system. And it is called as component diffusion decoupling only when the diffusivities difference is more than factor two, because diffusivities difference of less than factor two normally originates from radius and mass differences, as described in section 2.3.1. Another decoupling terminology is viscosity decoupling which is the difference between the measured self-diffusivity and the diffusivity converted from viscosity measurement using Stokes-Einstein relation in Eq. (2-2).

The background of the present work is the previous investigation in multicomponent Pd-based, $Pd_{43}Cu_{27}Ni_{10}P_{20}$, glass forming system [17]. It has been

shown in this investigation that there is no component diffusion decoupling between larger and smaller components in the melt regime and above the critical temperature, T_c, of MCT. Below T_c, however, very significant component diffusion decoupling between the larger and smaller components is observed. This is because when the system enters supercooled and glassy regime, the atoms have to overcome high activation barriers by local hopping and the diffusivity of the larger atom differs from the diffusivities of the smaller atoms by many orders of magnitude. This result is in accord with MCT prediction about the onset of liquid-like motion at T_c.

It is interesting to know whether the above mentioned investigation result in multicomponent Pd-based melt is also generally accepted for another glass former melts. Although $Pd_{43}Cu_{27}Ni_{10}P_{20}$ alloy is still considered as the best known metallic glass former so far [2], Pd is a very expensive element and thus it is not very realistic to be used in industry. Therefore, in the present investigation, the study is extended to multicomponent Zr-based glass former melt which contains cheaper elements and is more realistic to be used in industry.

It has been well known for long time that multicomponent is the prerequisite for good glass forming ability (GFA) as stated in "confusion principle" to produce bulk metallic glasses (BMGs). Normally, the simpler the alloy systems, the more difficult the BMGs are produced. Thus, it is interesting to understand the influence of system complexity to the diffusion of atoms in the melt of the respective system. Hence, this study is further extended to the melt of simpler alloy systems in order to understand the atomic diffusion in melt of multicomponent system.

2.4.1 Aim of the study

As mentioned before, there are two goals needed to be achieved in the present work. The first goal is we want to see whether the result in multicomponent Pd-based systems is generally accepted also in multicomponent Zr-based systems. And the

second is to understand the diffusion processes in multicomponent Zr-based melts. Therefore, in order to accomplish these goals, this work is divided in to two parts:

Part I is radiotracer diffusion measurement of ^{95}Zr and ^{57}Co in multicomponent Zr-Ti-Cu-Ni-Be system above the liquidus temperature, T_l. ^{57}Co is used as a substitute for Ni which represents the smaller components.

Part II is the same measurement as in *Part I*, but in simpler systems, i.e. binary and ternary Zr-Ni(-Al) systems, in order to understand the diffusion process of Zr and Ni in the multicomponent Zr-based glass forming melts.

From the result of this investigation, we expect that we can explain the component diffusion decoupling, i.e. the difference between Zr and Ni diffusivities, in Zr-based glass forming melts in terms of potential energy landscape point of view, mode coupling theory (MCT) and atomic connectivity network. The viscosity decoupling will also be discussed by comparing the measured diffusivities with diffusivity converted from viscosity by Stokes-Einstein relation. In addition, from the experimental results in Part II, we expect that we can explain the influence of the size effects and the existence of pronounce CSRO in the structure on the Zr and Ni diffusion decoupling behaviour, particularly in binary Zr-Ni melts. In this part of investigation, the agreement with the recent hard-sphere and MCT studies in binary Zr-rich melts will also be given. Additionally, the ^{57}Co diffusivities, measured in the present investigation, are compared with the Ni diffusivity measured by quasielastic neutron scattering (QNS) to ensure the measurement is not affected by convection. In this case, ^{57}Co is used as a substitute for Ni which represents the smaller components [43].

2.4.2 Alloy systems being studied

In this investigation, four types of alloy systems are used. In Part I, one multicomponent Zr-based system with chemical composition $Zr_{46.75}Ti_{8.25}Cu_{7.5}Ni_{10}Be_{27.5}$ are used. This alloy has been commercialized by Liquidmetal® Technologies with commercial name Vitreloy 4 (Vit 4). It is known to have a good GFA with a critical cooling rate of about 1 K/s [44]. However, although it is considered as one of the best BMGs and Zr is cheaper element, this alloy contains Be which is considered toxic.

In Part II, three different simpler alloy systems are investigated, i.e. binary $Zr_{64}Ni_{36}$ and $Zr_{36}Ni_{64}$, and ternary $Zr_{60}Ni_{25}Al_{15}$. The first two are categorized as conventional metallic glasses which are bad glass formers and need a high cooling rate of more than 105 K/s for vitrification. The ternary alloy $Zr_{60}Ni_{25}Al_{15}$ can be produced with a critical cooling rate of less than 100 K/s [45].

The following is some characteristics of all alloy systems used in Part I and Part II. This information will be very useful later for data analysis of the experiments.

- **Liquidus temperature**

As the aim of the investigation is radiotracer diffusion measurement in the melt regime, and as a melt is an equilibrium phase, the only characteristic temperature relevant for this investigation is the liquidus temperature, T_l. T_l can be measured using differential scanning calorimetry (DSC) or differential thermal analysis (DTA). As all samples were prepared by the working group of Prof. Andreas Meyer in German Aerospace Centre (DLR) in Cologne, the liquidus temperatures of the alloys used in the present investigation refer to the their work. T_l of Vit. 4 is 1050 K [46], and T_l of $Zr_{64}Ni_{36}$, $Zr_{36}Ni_{64}$ and $Zr_{60}Ni_{25}Al_{15}$ are 1283 K, 1343 K and 1215 K, respectively [10].

- **Viscosity**

Viscosity can be determined by measuring the decay time constant of free oscillation of a sample droplet levitated using electrostatic levitation (ESL) techniques, which details can be found elsewhere [47]. The viscosity of Vit. 4, $Zr_{64}Ni_{36}$, $Zr_{36}Ni_{64}$ and $Zr_{60}Ni_{25}Al_{15}$ can be seen in Figure 2-5. Viscosity measurement is very useful when the validity of Stokes-Einstein relation, as described in section 2.1.3, has to be checked. As seen in this figure, the viscosity of the respective melts fits Vogel-Fulcher-Tammann equation (Eq. 2-12) well. Additionally, the viscosity of Vit. 4 is not significantly different from the viscosity of the binary $Zr_{64}Ni_{36}$, the viscosity of $Zr_{60}Ni_{25}Al_{15}$ is higher than the viscosity of $Zr_{64}Ni_{36}$, and the viscosity of $Zr_{36}Ni_{64}$ is the highest of all.

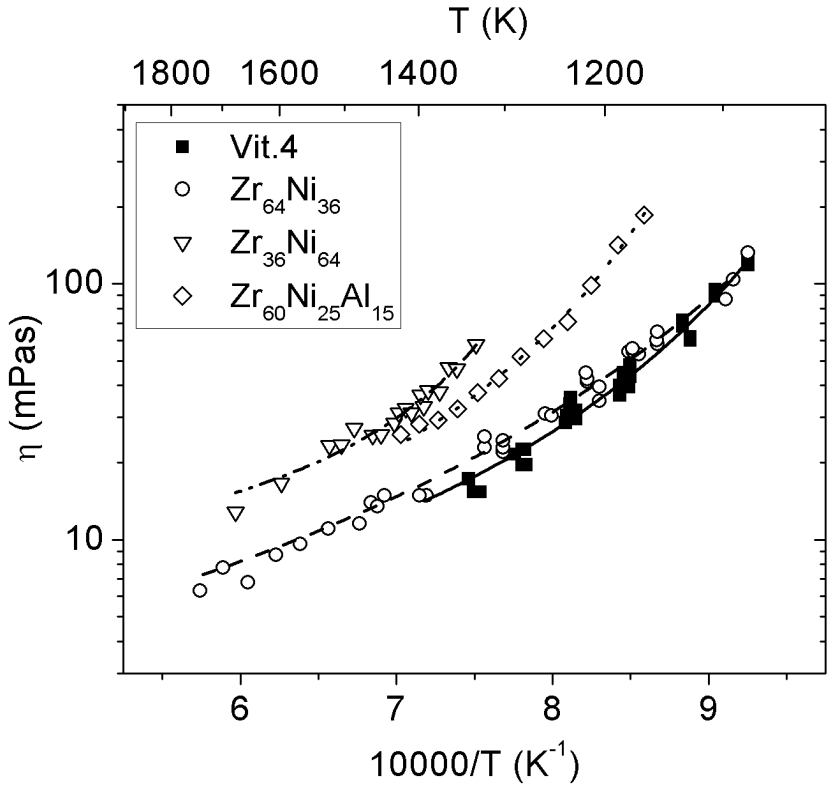

Figure 2-5 Temperature dependence of viscosities of Vit. 4 [7], $Zr_{64}Ni_{36}$ [47], $Zr_{36}Ni_{64}$ and $Zr_{60}Ni_{25}Al_{15}$ melts [Fan, from private communication in 2014]. The lines represent the Vogel-Fulcher-Tammann fit of the viscosity of the respective melts

- **Diffusivities from quasielastic neutron scattering**

Figure 2-6 shows the dependence of Ni diffusivities in $Zr_{64}Ni_{36}$, $Zr_{36}Ni_{64}$ and $Zr_{60}Ni_{25}Al_{15}$ melts [10] and of Ni and Ti in Vit. 4 melt [9] which were measured using quasielastic neutron scattering (QNS) method. The working principle of QNS will be mentioned briefly in section 2.4.3, and details can be found elsewhere [9-10, 19]. As seen in this figure, Ni diffusivities of Vit. 4 and $Zr_{64}Ni_{36}$ are also the same (see their viscosities data above, they also have similar viscosities). This may indicate similar diffusion mechanism. Furthermore, the Ni diffusivities in $Zr_{36}Ni_{64}$ and in $Zr_{60}Ni_{25}Al_{15}$ are not significantly different, and they are significantly lower than the Ni diffusivities in $Zr_{64}Ni_{36}$ and in Vit. 4.

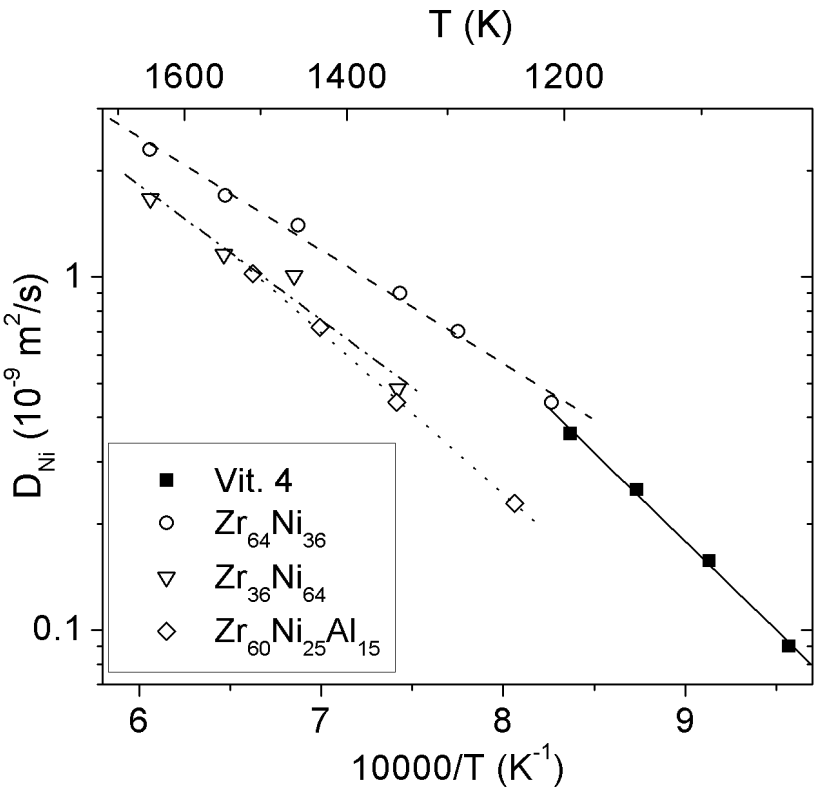

Figure 2-6 Temperature dependence of Ni diffusivities in $Zr_{64}Ni_{36}$, $Zr_{36}Ni_{64}$ and $Zr_{60}Ni_{25}Al_{15}$ melts [10] and of Ni and Ti diffusivities in Vit. 4 melt. The linear lines are drawn to guide the eye.

- **Chemical short range order**

Figure 2-7 shows a complete set of partial structure factors which have been measured experimentally in Zr-rich $Zr_{64}Ni_{36}$ melt at 1375 K by neutron scattering [48]. The prepeak feature in S_{NiNi} is the evidence of chemical short range order (CSRO) in this melt. A complete set of partial structure factors in the melt of $Zr_{36}Ni_{64}$ has also been measured by German Aerospace Center (DLR) [Fan, from private communication in 2014][*] and also has shown the evidence of CSRO.

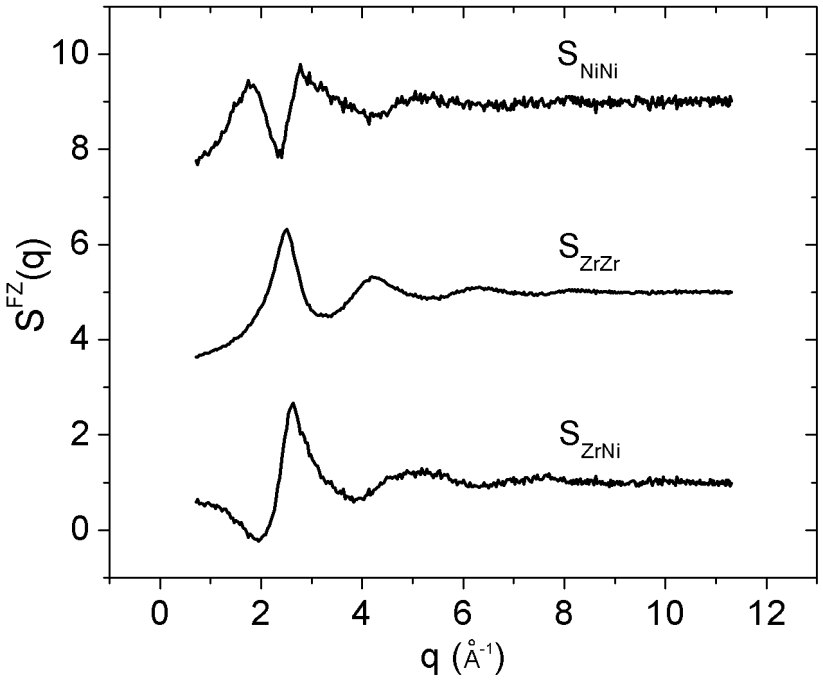

Figure 2-7 Partial static structure factors of $Zr_{64}Ni_{36}$ melts at 1375 K [48].

According to our knowledge, there is no experimental study on the complete description of the structure of $Zr_{60}Ni_{25}Al_{15}$ melt so far. But a molecular dynamic simulation on amorphous $Zr_{60}Ni_{25}Al_{15}$ has been reported and has also shown the evidence of a complex CSRO around Ni and Al [49].

[*] The results are not shown here because they are not yet published.

- **Packing density**

Packing fraction (or packing density) provides information about how dense atoms are packed in the melt. Packing fraction is defined as

$$\varphi = \frac{V_A}{V_m} \qquad (2\text{-}13)$$

the ratio of atomic volume (V_A) and the average volume available for an atom, usually called as molar volume (V_m) [8]. The value of V_m is calculated from the macroscopic density ρ of the melt as

$$V_m = \frac{M}{N_A \rho} \qquad (2\text{-}14)$$

with N_A is Avogadro number, M is the relative molar mass of the alloy and ρ is the macroscopic density.

If atoms are assumed to be hard-sphere-like, the value of V_A is calculated from the corresponding atomic radii [50] (r_{Zr} = 1.45 Å, r_{Ni} = 1.15 Å, r_{Al} = 1.25 Å, r_{Cu} = 1.17 Å, r_{Ti} = 1.32 Å, r_{Be} = 0.89 Å) by $V_A = \frac{4}{3}\pi r^3$. However, when chemical short range order (CSRO) exists in the structure of the melt, the calculation of V_A using hard-sphere radii can lead to the wrong value. CSRO is known to cause anomaly in the composition dependence of the atomic volume [40, 51]. Therefore, the V_m can be qualitatively used to describe the packing density in system with CSRO [8, 39], if it is assumed that the packing density is independent of the number of the components. As V_m is calculated from the macroscopic density, ρ, according to Eq. (2-2), one needs to have the information about the macroscopic density. The macroscopic densities of Vit. 4, $Zr_{64}Ni_{36}$, $Zr_{36}Ni_{64}$ and $Zr_{60}Ni_{25}Al_{15}$ which are shown in Figure 2-8b were obtained from the private communication with Dr. Fan Yang in 2014 from DLR.

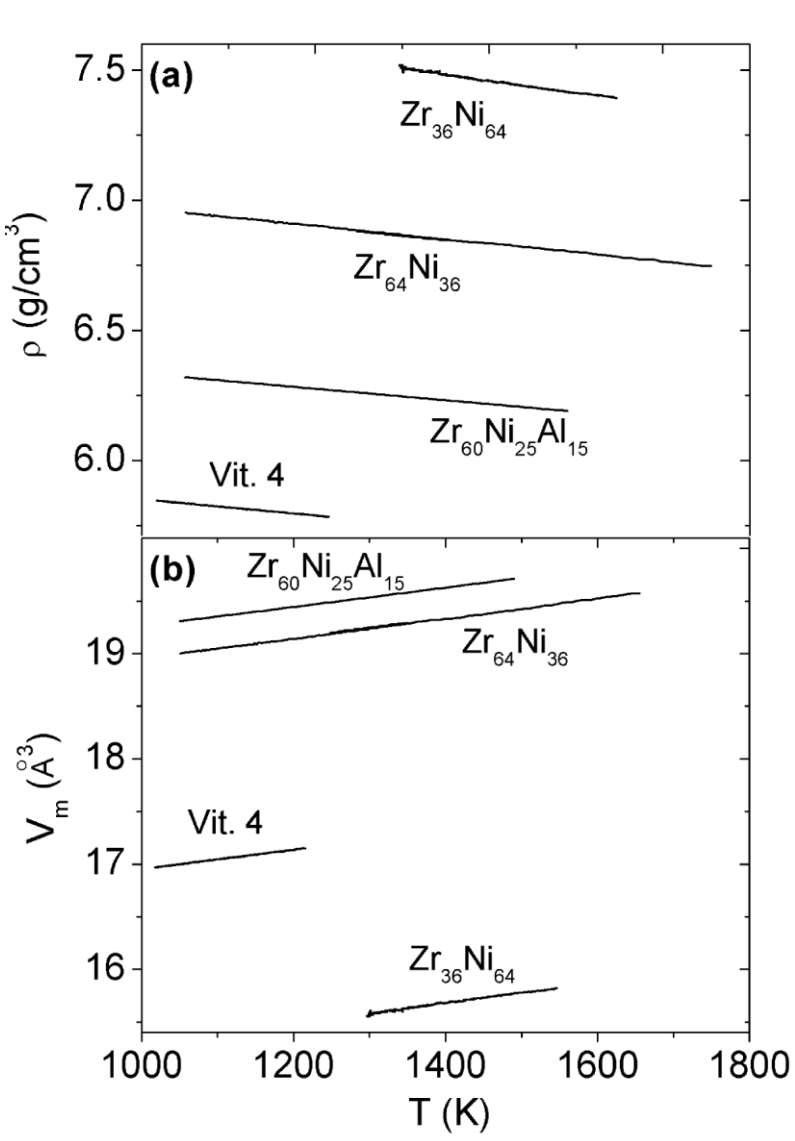

Figure 2-8 (a) the density and (b) the calculated molar volumes of Vit. 4, $Zr_{64}Ni_{36}$, $Zr_{36}Ni_{64}$ and $Zr_{60}Ni_{25}Al_{15}$ which are plotted against temperatures.

Figure 2-8b above shows also the V_m of the respective melts which is plotted against temperatures. The larger the V_m, the lower the packing density is. The higher packing density of the $Zr_{36}Ni_{64}$ than that of $Zr_{64}Ni_{36}$, the as seen in this figure, is expected because the more number the smaller atoms, Ni, are added into the system, the denser the system will be. If it is assumed that packing density is independent of the number of the components, the packing density of Vit. 4 is in between the packing

density of the binary Zr-Ni systems, and the packing density of $Zr_{60}Ni_{25}Al_{15}$ is the lowest.

- **MCT study on real system and on hard-sphere model of $Zr_{64}Ni_{36}$**

Hard-sphere model show purely an entropic mixing. Therefore in hard-sphere model, the chemical interaction effects which can be visualized from the evidence of CSRO can be excluded and only packing density is considered. In real system, however, it is not only packing density but also chemical interaction which can influence the transport properties of a system. And as MCT is known to be true in the melt, it can be used to calculate the relative diffusivities of the melt atomic constituents with using the input of the structure factor of the respective melt, although it cannot predict the absolute value of the diffusivities [16].

Melts of metallic glass formers are mostly highly dense systems. And it has been reported that diffusion of atoms in dense metallic melts is similar to hard-sphere systems. Melts with high packing density tend to have sluggish dynamics, or low diffusivities [8, 14-15]. In addition, MCT study for hard-sphere model of $Zr_{64}Ni_{36}$ melt has also shown that diffusivities between the large and the small atom are different by about a factor of two [16]. However, the MCT study on the real system of $Zr_{64}Ni_{36}$ has shown that diffusivities of Zr are the same as Ni diffusivities [16]. Therefore, it has been suggested from this study that CSRO, which exists in the structure of $Zr_{64}Ni_{36}$ melt, reduces the component diffusion decoupling in $Zr_{64}Ni_{36}$ melt.

2.4.3 Diffusion measurement techniques

Nowadays, there are a lot of techniques which have been developed to measure diffusivity [19, 52]. However only those relevant to the present work will be explained in this dissertation. They are radiotracer diffusion measurement and quasi-elastic neutron scattering (QNS).

- **Radiotracer diffusion measurement**

Radiotracer diffusion measurement technique is a method of determining diffusivity of a very little amount of labelled atom with its radioactive isotope in a matrix containing (self-diffusion) or not containing (impurity diffusion) that atom. It is categorized as one of the direct diffusion measurement methods. This method is quite superior to other diffusion techniques due to high sensitivity of gamma ray spectrometers. As this technique requires only very little amount of tracer in order to determine either self- or impurity diffusivity, the tracer can diffuse without changing the composition of the sample matrix since chemical potential difference plays no role and the thermodynamic factor is equal to one [19].

In radiotracer technique, the tracer is deposited in a very thin film as compared to the diffusion length. Therefore, diffusivity value D is calculated according to the thin film solution of Fick's second law in Eq. (2-5) which is

$$C(x,t) = \frac{M}{\sqrt{\pi Dt}} \exp\left(\frac{-x^2}{4Dt}\right) \qquad (2\text{-}15)$$

for thin film geometry and

$$C(x,t) = \frac{M}{2\sqrt{\pi Dt}} \exp\left(\frac{-x^2}{4Dt}\right) \qquad (2\text{-}16)$$

for sandwich geometry with t is the diffusion time, x is the penetration depth and M is the number of diffusing particles per unite area. In Eq. (2-11) and (2-12), one would notice that these solutions are all Gaussian solutions. The diffusion length is characterized by the value $2\sqrt{Dt}$.

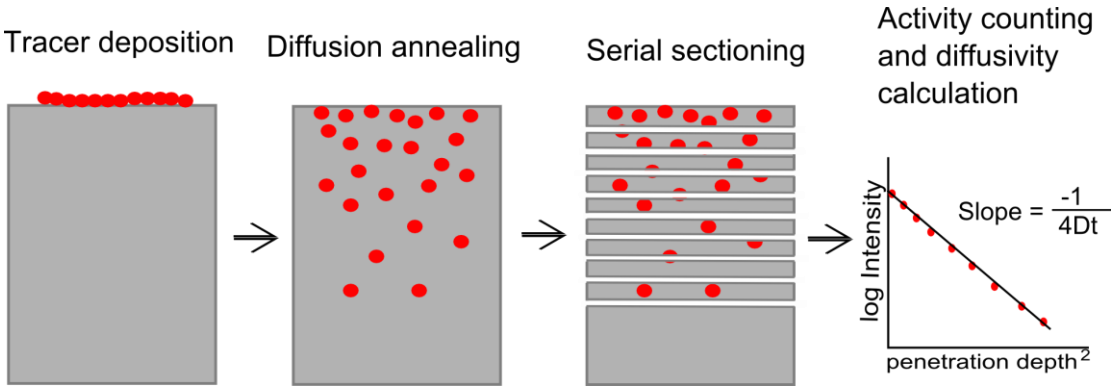

Figure 2-9 Schematic of the sequence of radiotracer diffusion measurement technique using thin film solution of Fick's second law

Radiotracer diffusion measurement technique involves some sequence of processes as shown schematically in Figure 2-9. After deposition of the very small amount of radiotracer, the sample is annealed at the investigation temperature to let the tracer diffuse into the matrix of the sample. After cooling, the sample is divided into layers (serial sectioning) using techniques according to the length of the penetration depth of the tracer into the sample. When the penetration length is very long as it is the case in the present work, the serial sectioning is done by mechanical grinding. The concentration of the tracer in each layer is then counted using gamma spectroscopy. After counting the activity of the tracer in all layers, a plot of $\ln C(x,t)$ versus x^2 can be drawn and diffusivity, D, can be calculated by $D = -1/(4t \cdot slope)$ according to Eq. (2-15) and (2-16).

- **Quasi-elastic neutron scattering (QNS)**

Quasi-elastic neutron scattering (QNS) is one of the indirect diffusion measurement techniques which have been used for understanding diffusion processes on a microscopic level. Diffusion of atoms in samples with suitable scattering cross sections can be studied using QNS technique if a high resolution neutron spectrometer is used. This technique is applicable only to relatively fast diffusion process with jump distance and diffusion path are in a range comparable to the neutron wavelength which is between 10^{-8} and 10^{-10} m [19]. Diffusion measurement using QNS technique depends on the incoherent scattering contribution to the total scattering cross section. The measurement is based on the broadening of the incoherent quasi-elastic neutron scattering signal width (or full width at half maximum) Γ_{inc} from which self diffusivity can be calculated by $D = \Gamma_{inc} q^{-2} / 2\hbar$ [10, 19, 39], where q is the wave vector transfer and $\hbar$ is Planck's constant. Technical details about diffusion measurement using QNS can be found elsewhere [19, 39].

Chapter 3 Experimental method

In this Chapter, the experimental details are given. As it is mentioned in the introduction, the investigation is divided into two parts:

Part I Radiotracer diffusion measurement of ^{95}Zr and ^{57}Co in multicomponent $Zr_{46.75}Ti_{8.25}Cu_{7.5}Ni_{10}Be_{27.5}$ (Vit. 4) above T_l, and

Part II Radiotracer diffusion measurement of ^{95}Zr and ^{57}Co in simpler systems; binary Zr-rich $Zr_{64}Ni_{36}$ and Ni-rich $Zr_{36}Ni_{64}$[†], and ternary $Zr_{60}Ni_{25}Al_{15}$.

Both parts were using the same principle of radiotracer diffusion measurement as described in Section 2.4.3 and the same type of tracers. Only the sample geometry and the range of investigation temperatures were different due to different liquidus temperature T_l. In addition, the method of tracer deposition was also different because of the difference in sample geometry. For the sake of simplicity, experimental details of both parts will only be separated in the section where they are different, i.e. Section 3.1, Section 3.2 and Section 3.4. The reason why the sample geometry for *Part II* investigation should be different from the sample geometry for *Part I* is because of the much higher liquidus temperature, T_l, of the three simpler systems compare to that of Vit. 4, see section 2.4.2. As a consequence, the viscosity of those three systems is about factor four lower than that of Vit. 4 (see also section 2.4.2). Measurements of samples with very low viscosity can be easily affected by convective flow. Thus, sample geometry for *Part II* has to be long capillary to minimize the convection effects.

[†] Radiotracer diffusion measurements in the melt of Ni-rich $Zr_{36}Ni_{64}$ in this part were done by Elisabeth Gill as her master thesis.

3.1 Samples production

All samples were produced by the working group of Prof. Dr. Andreas Meyer at German Aerospace Center (DLR) Cologne, Germany. Therefore, all details about the sample production refers to their works [53]. The samples were prepared by standard suction casting, which involves rapid melting followed by introducing the resulting melt into a water-cooled cupper mould instantaneously by using a gas pressure. This method can produce a glassy metal ingot with a large size.

3.1.1 Sample production in *Part I*

For Part I, the ingot of multicomponent $Zr_{46.75}Ti_{8.25}Cu_{7.5}Ni_{10}Be_{27.5}$ (Vit. 4) was initially bought from Liquidmetal® Technologies. By DLR, this ingot was then re-melted and moulded into a rod with diameter of 8 mm using the method described above. After receiving the ingot from DLR, the sample was cut into 1 mm slices using a low speed diamond saw, followed by polishing one side into mirror like.

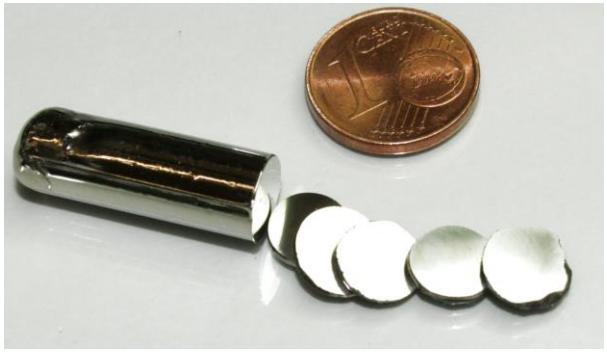

Figure 3-1 Rod of Vit.4 with diameter of 8 mm, and some slices of the sample with thickness of 1 mm

3.1.2 Sample production in *Part II*

For Part II, the samples of compositions $Zr_{64}Ni_{36}$, $Zr_{36}Ni_{64}$ and $Zr_{60}Ni_{25}Al_{15}$ were produced from the constituents by using suction casting described above. From this procedure, long capillary rods with diameter of 1.5 mm and length of 15 mm were

produced. After receiving the sample from DLR, it was polished mirror like on one side of each rods.

3.2 Radioactive tracers

3.2.1 ^{57}Co

^{57}Co is one of radioactive isotopes of cobalt (Co) with half-life time to be the second longest after ^{60}Co. The half-life time of ^{60}Co is 5.27 years and the half-life time of ^{57}Co is 271.9 days. The other of Co radioactive isotopes have half-life time less than 80 days which is not convenient to be used for this analysis. The very long half-life time of ^{60}Co is also not desired to be used in laboratory because of storing issues, in addition to the beta particle emission which can cause trouble during handling. ^{57}Co decays into stable ^{57}Fe by electron capture accompanied by gamma emission with an energy of 122 keV (85.6 %) and 136.5 keV (10.7%) which can be clearly identified using gamma spectroscopy.

^{57}Co tracer was supplied by Eckert & Ziegler Braunschweig, Germany, in the form of 5 ml solution of 0.1 M $CoCl_2$ in HCl with 37 MBq activity as it was received. This solution was used as a tracer source of ^{57}Co as substitute for Ni for all samples being investigated here. The reason why ^{57}Co was used instead of Ni isotopes was because there is only one radioactive isotope of Ni which can be feasibly used, i.e. ^{63}Ni. The other radioactive isotopes of Ni have half-life time less than 10 days which is too short to be used for analysis. However, ^{63}Ni is not convenient to be used too. It is again because of its very long half-life time which is 100 years and the emission of beta particles. Additionally, radiotracer experiments with ^{57}Co have had comparable results with the diffusivities of Ni measured using secondary-ion mass spectroscopy (SIMS) [54].

3.2.2 ^{95}Zr

^{95}Zr tracer has a half-life time of 64 days. It decays into radioactive ^{95}Nb by emitting beta minus particle and accompanied by emission of gamma rays with an energy of 724.20 keV (44%) and 756.73 keV (54%). It is then followed by the decays of the daughter ^{95}Nb, with a half-life time of 35 days, into the stable isotope ^{95}Mo by emitting another beta minus particle followed by gamma radiation with energy 765.8 keV (100%). Since the decay mode is emission of beta minus, the material should be handled with care. There is ^{88}Zr which has a little longer half-life time of 83.4 days and decays into ^{88}Y by electron capture. However, ^{88}Y is also an active isotope. The isomer of this isotope emits gamma rays with the same energy as the gamma rays emitted by ^{88}Zr, i.e. 393 keV. Hence, choosing ^{88}Zr as the tracer to probe Zr atom diffusivity is not a good idea.

It is not the first time to use ^{95}Zr as a tracer here. The preparation procedure for ^{95}Zr as a tracer is already well established [43, 55]. As stated in the previous works, the form of ^{94}Zr is metallic powder. However, the metallic powder of ^{94}Zr was not available anymore on the market when the present project was started. Hence, we used the oxide powder form of ^{94}Zr which was supplied by *Chemotrade Chemiehandelsgesellschaft mbH*, especially for the diffusivity determination in Vit. 4 melt. Later, we found a supplier which could provide ^{94}Zr in the form of crystalline plates which were supplied by Oak Ridge National Laboratory USA. We used the later form mostly for determination of diffusivity in binary and ternary Zr-Ni(-Al) melts.

The irradiation of inactive ^{94}Zr, either in the form of metallic powder (plate) or in the form of oxide powder, to active ^{95}Zr was done by Hahn-Meitner-Institut (HMI) Berlin with procedure the same as the previous work [55]. As the next step will involve the use of hydrofluoric acid (HF), the inactive powder was stored in a 2 ml

Eppendorf Safe-Lock Tube™ made of polypropylene. In this way, the handling was much easier because there was no need to transfer the powder (or plates) containing very high activity of ^{95}Zr from quartz tube to polypropylene tube.

3.3 Tracer deposition techniques

Since most of the radioactive material is available commercially in solution, evaporation, electrochemical deposition, and drop casting are most common techniques for tracer deposition. It has to be noted that a homogeneous thin film surface is not really an important aspect here as long as the thickness irregularity is small compare to the average diffusion length and as long as the same area is counted in each section [19].

As mentioned earlier, the tracer deposition technique for *Part II* should be different from *Part I* because of geometry problem. The very narrow surface area and the high aspect ratio of the samples used in *Part II* makes it impossible to deposit the tracers in the same way as in *Part I*.

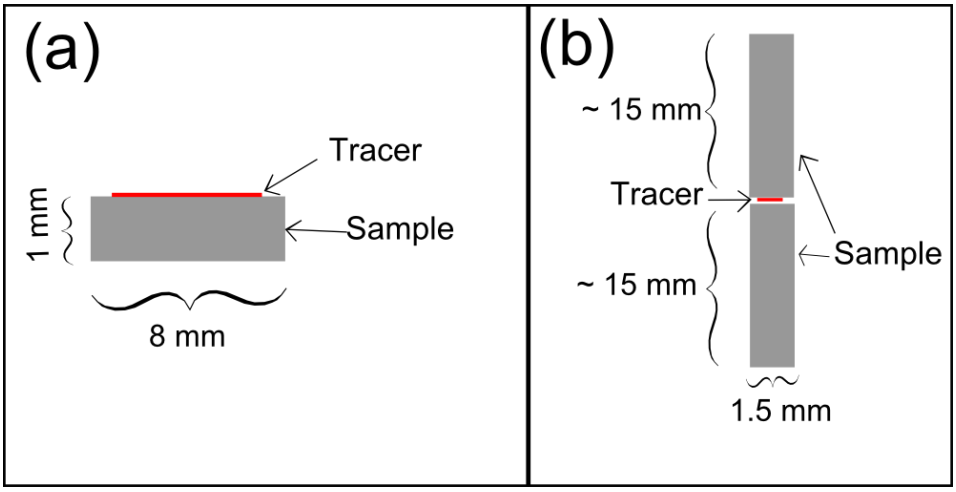

Figure 3-2 Illustration of the geometry and the initial conditions of the samples used for the diffusivity measurement in this investigation: (a) thin film geometry used for experiment in vitreloy 4. and (b) sandwich geometry used for experiment in binary and ternary $Zr-Ni(-Al)$ systems in a capillary graphite crucible.

3.3.3 Tracer deposition in *Part I*

The deposition methods of ^{57}Co and ^{94}Zr tracers used in *Part I* of this investigation have been well established previously. Therefore the technical drawing of the apparatus should refer to the previous work [55]. Here, only the basic principle of the methods and anything new related to the procedures is given. See Figure 3-2a for the description of sample geometry and the position of the tracer film.

- **Deposition of ^{57}Co by evaporation**

Evaporation deposition technique is a method to transfer atoms from a hot source to a cold substrate by thermal means in vacuum environment [56].

About 70 μl - 100 μl of solution containing ^{57}Co (see Section 3.2.1) with activity of about 500 kBq was dropped on a tungsten boat of an evaporator, where it was evaporated and deposited on top of the sample surface (See the previous work for details [55]). This procedure should create a thin film containing ^{57}Co tracer with thickness of about few hundreds nm with specific activity of less than 1.25 $kBq/\mu g$.

- **Deposition of ^{95}Zr by electrochemical deposition**

Electrochemical deposition is a chemical deposition method which involves oxidation and reduction reaction. The basic principle of the method is the reduction of a metal ion contained in a electrolyte solution into its metallic form by electron transfer with the help of electric current. Detailed drawings of the apparatus can be seen in the previous work [55].

In order to do electrochemical deposition, the first thing one needs is to produce an electrolyte solution containing ^{95}Zr ions. The solution was prepared by dissolving the active powder (or plates) in 40 μl hydrogen fluoric acid (HF) 40%. When the metallic form of Zr is used, the reaction of HF is spontaneous. This reaction will produce ZrF_4 and release hydrogen gas. However, when the oxide form

is used, the complete reaction with HF will take at least 1 week. This is because the enthalpy of reaction between ZrO_2 and HF is higher than that between metallic Zr and HF. In the reduction process of Zr^{4+} into Zr using electrochemical deposition method, if water is present inside the electrolyte solution, water will be reduced first instead of the Zr^{4+} ion. Therefore, 1 ml of dimethylsulfoxide ($DMSO$) was added in order to destroy the structure of water [57]. The total reaction which occurs during electrochemical process is

Reduction process at cathode (-): $Zr^{4+} + 4e^- \rightarrow Zr(s)$	$E^o = \text{-}1.45 V$ [58]
Oxidation process at anode (+): $2F^- \rightarrow F_2(g) + 2e^-$	$E^o = \text{-}2.87 V$ [58]
Total reaction: $Zr^{4+} + 4F^- \rightarrow Zr(s) + 2F_2(g)$	$E^o = \text{-}7.19 V$

And the amount of Zr deposited on top of the sample can be calculated using Faraday's first law described as

$$m = \left(\frac{q_i}{F}\right)\left(\frac{M}{z}\right) \qquad (3\text{-}1)$$

where m is the mass of Zr deposited on top of the sample, $q_i = It$ is the total electric charge which is equal to the total amount of current at a certain time. F is the Faraday constant which is equal to 96485 $C\,mol^{-1}$, M is the atomic mass of Zr and z is 4 which is the number of electrons needed to convert Zr^{4+} into Zr. During the present investigation, the current of < 16 mA which produced from applied voltage of 40 V was let flown for $3\,s$ through 20 μl of the electrolyte which was dropped on top of the sample. The drop of the electrolyte solution creates a droplet with diameter of approximately 6 mm. This technique will create about tens nm thick Zr film containing ^{95}Zr tracer on top of the sample with specific activity of less than 400 $Bq/\mu g$.

3.3.4 Tracer deposition in *Part II*

For samples with high aspect ratio and small diameter such as the samples used for *Part II*, drop casting is the best way to deposit the both radiotracers, ^{57}Co and ^{95}Zr . Drop casting involves dropping a solution on top of a substrate followed by drying process to evaporate the solvent.

All diffusivity measurements of ^{57}Co and ^{95}Zr tracers done in Part II were simultaneous diffusion measurements. And drop casting has the advantage of mixing the two tracer solutions homogeneously. The two solutions containing ^{57}Co and ^{95}Zr described in Section 3.2 above were mixed with ratio 1:1. $1\ \mu l$ of this mixture was dropped on top of the polished mirror-like sample. In order to guide the droplet to be in the centre of the sample and no contamination at the side of the sample, the sample was masked with parafilm® with a hole of about $0.8\ mm$ diameter at the centre of the sample. Because of the hydrophobicity of the parafilm® and the hydrophilicity of the tracers solution, the droplet forms an almost perfect sphere. This allow us to drop high volume of solution without dripping the solution to the side of the sample. Complete drying of the droplet was done using an infrared lamp for about 2 hours. After drying, a film with a thickness of a few μm and with specific activity of less than $5\ kBq/\mu g$ was produced (see Figure 3-2b for the description of sample geometry and the position of the tracer film).

3.4 Diffusion annealing

After the tracers deposition, the sample was put inside a graphite furnace with suitable geometry, and isothermally heated at temperatures above the liquidus temperature of each alloy systems. As mentioned earlier, due to the much higher liquidus temperature of samples used in Part II, and as well as the different sample geometry, a different design of furnace was made for this investigation.

3.5.1 Diffusion annealing in *Part I*

- **Crucible**

The crucible used for diffusion annealing in Part I was made of graphite with geometry as in Figure 3-3. As the sample contains Zr element, and as this element is very reactive in particular at high temperature, it could react with the crucible material during annealing. To prevent this reaction, the inner side of the graphite was coated with Pyropaint^{TM} 634-AS supplied by KAGER Industrieprodukte GmbH (see also Figure 3-3). The coating material was applied using a brush. After drying, the coated surface of the lid was polished to provide smooth surface to reduce irregularities of the sample after annealing.

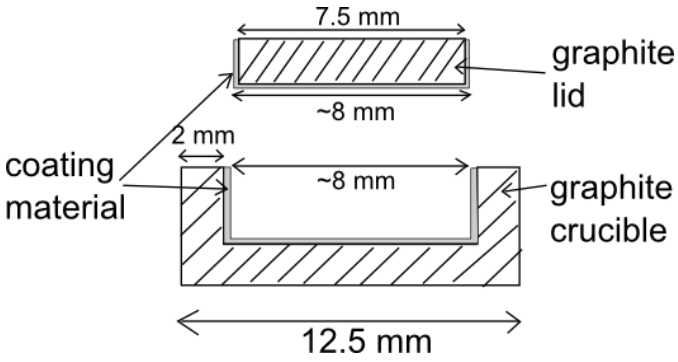

Figure 3-3 Vertical cross section of the graphite crucible used in Part I, coated with Pyro-paint^{TM} 634-AS

- **Furnace**

As the T_l of Vit. 4 is only 1050 K, annealing in this part was done using the same furnace as it was used in the previous work, it was called Toaster furnace. The technical drawing of this furnace can be found in the previous work [55].

- **Annealing profile**

Samples in Part I (Vit. 4) were annealed at temperatures between 1050 K to 1130 K. Annealing was done under vacuum of about ~ 10^{-7} mbar. Typical annealing profile used in this part can be seen in Figure 3-6a. The temperature measurement was done using a thermocouple Type K with a standard error of 0.75 %. The measurement of the temperature during annealing has a statistical error of less than 2 K which is calculated with 95% confidence level. The temperature was measured on the outer surface of the graphite crucible because it is not possible to do measurement directly on the sample inside the crucible in this way. The correction of the measured temperature was done by subtracting the measured temperature with the temperature difference between the outer side and the inner side of the graphite crucible after coated with the coating material, which is 40 K. This was done separately and the value consists a large measurement uncertainty of about 10 K, because the thickness of the coating material was not controlled.

3.5.2 Diffusion annealing in *Part II*

- **Crucible**

The crucible used for diffusion annealing in this part was made of high density graphite with geometry as in Figure 3-4. Because the annealing temperatures in Part II were much higher that in Part I (above 1200 K), reaction between sample and crucible could still occur even when the crucible has been coated with Pyropaint^{TM} 634-AS. Therefore, yttrium oxide (Y_2O_3) in ethanol suspension was used as the coating material, which was supplied by Sindlhauser Materials GmbH. The coating was applied on the inner side of the crucible tube by filling the suspension inside the tube followed by blowing using a syringe. This was done twice to get a thickness of some tens μm.

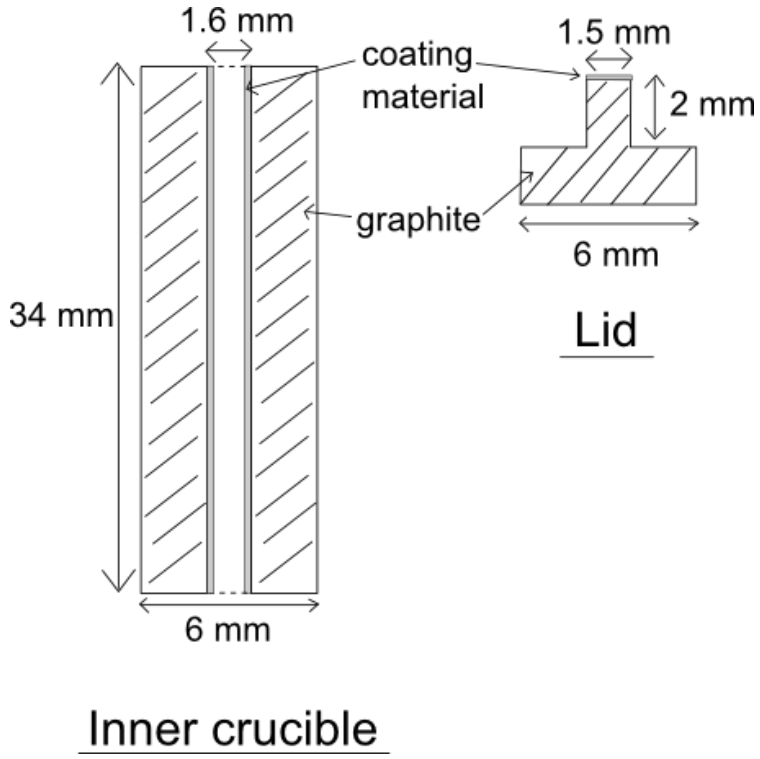

Figure 3-4 Illustration of inner crucible used for Part I. It also shows the coating layer using Y_2O_3

- **Furnace**

As mentioned earlier, new design of furnace which can accommodate very high temperature (above 1200 K) should be established in order to perform investigation Part II. Another requirement needed for the application in this Part is that there should be no or very less temperature gradient between top and bottom of the crucible. Otherwise, convective flow may occur. The improved new design furnace was adapted from the furnace developed by DLR which they used for inter-diffusion experiment, as seen in

Figure 3-5.

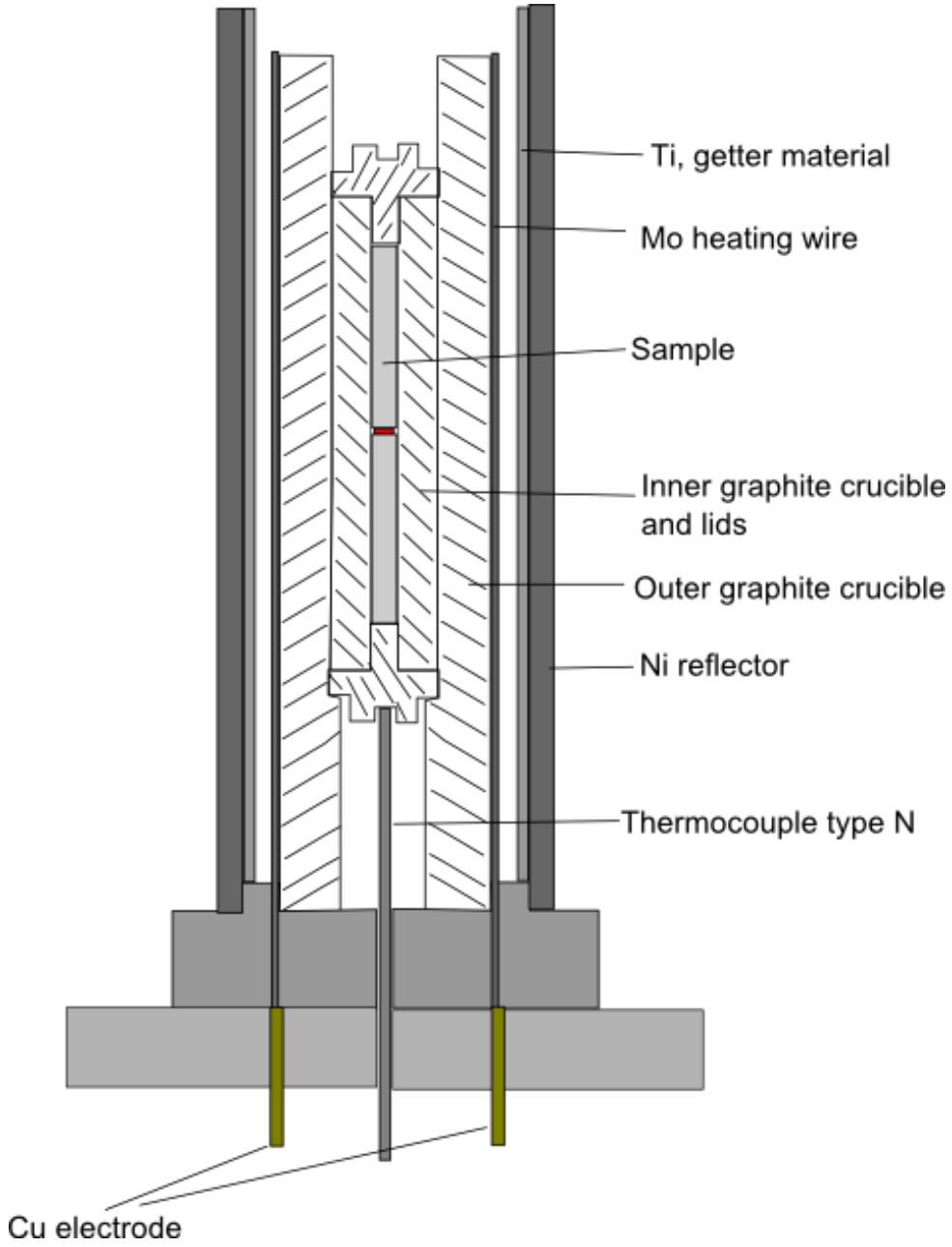

Figure 3-5 Illustration of the furnace used for investigation Part II

Some features which are in this furnace but not in Toaster furnace are the smaller size, using high density graphite, conductive heating transfer through graphite, and using titanium (Ti) getter material. The first three were meant to increase the high temperature performance and the temperature homogeneity along the crucible. While the getter material was used to minimize the oxidation of *Mo* wire.

Mo wire was used because it can be bent easily compared to W wire. However, molybdenum dioxide, MoO_2, which is formed after oxidation of Mo has quite low melting point of $1373\,K$, which is lower than the annealing temperature of the binary and ternary systems being investigated here. This will cause the furnace cannot be used after few heating cycles. This problem was solved by putting getter material, i.e. Ti, and using high vacuum (10^{-5} - $10^{-8}\,mBar$) chamber which can slow down the oxidation process of the wire, and hence increases the life time of the furnace.

The furnace was temperature calibrated by measuring the melting point of pure silver (Ag), which is at around 1235 K. And the temperature difference between top and bottom of the crucible was checked by inserting a second thermocouple (type K) from the top of the furnace, and it was not more than 2 K.

- **Temperature profile**

A sample with radiotracer on it was connected with the other half of the rod resembling a sandwich geometry as seen in

Figure 3-5, and inserted into the inner crucible. Annealing was performed at temperatures between 1290 K - 1488 K. The typical annealing temperature profile can be seen in Figure 3-6b. The sample was held at constant temperature at about 600 K to let all parts to gas out to avoid oxidation of Mo wire. Mo wire starts to oxidize at temperatures around 770 K.

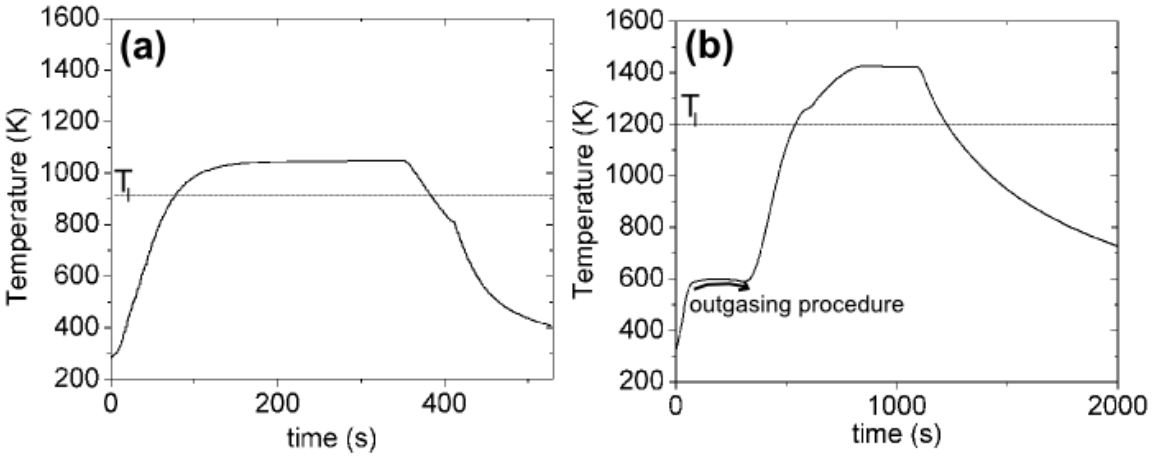

Figure 3-6 Typical annealing temperature profiles in (a) Part I and (b) Part II

The temperature was measured using a thermocouple type N, with a standard error of 0.75 %. The measurement of the temperature during annealing has a statistical error of less than 2 K which is calculated with 95% confidence level. As seen in Figure 3-6, the temperature was measured on the outer surface of the graphite crucible. The correction of the measured temperature was done by subtracting the measured temperature with the temperature difference between the outer side and the inner side of the graphite crucible after coated with the coating material, which is 15 K. This was done separately and the value consists measurement uncertainty of less than 5 K.

3.5 Serial sectioning

After annealing, the procedure is followed by serial sectioning of the samples into layers. As the diffusion length is quite large, about 200 - 300 μm for *Part I* and 1 - 2 mm for *Part II*, the serial sectioning can be done by mechanical grinding. The grinding was done by using alumina-based 3M lapping film which is commercially available, from A. S. T. Schleif-Technik GmbH, with alumina granule size of 30 μm

or 40 μm. The sample was grinded together with about 9 μl lubricant (Extender II from company San Dia) to keep the dust of the sample stick on the lapping film. Before and after grinding process, the sample should be weight to get the information about the total mass that is grinded for each layer thickness calculation. The masses were measured using an analytical balance Sartorius-MC5 with precision of 0.001 mg.

In order to calculate the thickness of each layer, one needs information about the density of the sample which can be calculated from the measurement of the sample mass divided by its volume. It was measured from a thick sample (of about 1 mm to 2 mm). The thickness was measured by calliper tool which has precision of 0.05 mm.

The penetration depth was calculated from the initial surface of the sample before it was grinded to middle point of each layer being grinded. Details about the grinding apparatus can be seen in the previous work [55].

3.6 Gamma spectroscopy

Gamma spectroscopy is a method to measure the energy and the intensity of gamma rays. In solid state gamma detectors, the measurement principle is based on the interaction of gamma rays with the active crystal of the detectors. The detector used in the present investigation is germanium (Ge) detector. When gamma rays interact with the active crystal of the detector, three possible effects will occur and lead to a typical spectrum. The first interaction will produce photo-electric effect. This effect occurs when gamma rays interact with tight-bound electrons, gives up all of its energy to electron and disappears. As a result, the electron will be ejected from the atom with a kinetic energy similar to the energy of the gamma rays. This effect contributes to a characteristic peak or photo peak in the spectrum of gamma energy. The second

interaction will produce Compton effect which leads to Compton background. The highest energy that can be deposited is called Compton edge. And the third way of interaction which is less important here is through pair-production.

A Ge detector was used to measure the energy and intensity of gamma rays emitted from the radiotracer ^{57}Co and ^{95}Zr with characteristic gamma energies already described in Section 3.2. A Ge detector is a semiconductor diode with a P-I-N structure. Any interactions, mentioned above, can occur in the intrinsic (I) region and can produce charge carriers (holes and electrons) which are swept to P and N electrodes by an electric field. The number of the charge carriers are proportional to the energy of gamma rays deposited in the detector and are converted to a voltage pulse by a charge-sensitive pre-amplifier. The pulse is then amplified by the amplifier, and analyzed by a pulse height analyzer. A multi channel analyzer will then map the pulse voltages into each respected channel numbers and count them. The result is displayed in a computer as a spectrum which shows the x-axis as the energy and the y-axis as the number of counts.

The activity is expressed as count per second (cps) and is proportional to the concentration of the tracers in each layer. And for further diffusivity calculation, this activity is then normalized with the thickness of each layer. According to Eq. (2-11) and Eq. (2-12), a plot of the normalized intensity in logarithmic scale versus the square of penetration depth will produce a linear line (see also Figure 2-9). The slope will be equal to

$$Slope = \frac{-1}{4D_{meas}t_l} \qquad (3\text{-}2)$$

in which the measured diffusivity D_{meas} can be calculated by inserting the time t_l which is the time of heating from liquidus temperature, T_l, to cooling back to T_l. The diffusivity during constant annealing time (D_{anneal}) is then calculated by multiplying D_{meas} with correction factor f as described in 3.7.

3.7 Correction factor for the measured diffusivity

When the annealing is done at very low heating rate, atoms diffuse already before the annealing temperature is reached. The annealing time is defined as the time when the temperature is constant. And diffusivity of the melt starting from its liquidus temperature, T_l, is normally significantly high. Therefore, the diffusion process from this temperature to the annealing temperature causes significant deviation of the measured diffusivity from true diffusivity at the annealing temperature. This is why correction of the measured diffusivity is needed. The correction can be done by assuming the temperature dependent diffusivity above T_l follows Arrhenius law. Although this is not particularly true because diffusion of atoms in the melt should not be influenced by activation energy which is usually the characteristic of Arrhenius law. However, as the temperature range of the measurement is not very large; it is only about 200 K, the temperature dependence diffusivity can be fitted with any law, for instance Arrhenius law. Therefore, by fitting diffusivity data in the melt of the respective alloy system measured by QNS [9-10] with Arrhenius equation in Eq. (2-6), fitting parameters, such as D_0 and E_a, can be obtained. Inserting these fitting parameters into the same Arrhenius equation but using the temperature profile used to anneal the samples, diffusivity ($D(T,t)$) profile over the measured time of the sample annealing process can be calculated.

The typical temperature profiles of Part I and Part II of this investigation can be seen in Figure 3-7a and Figure 3-7b. And the respective diffusivity profiles calculated from Eq. (2-6) are shown in Figure 3-7c and Figure 3-7d. In these figure, there are three area under the curve of $D(T,t)$ profile, marked as 1, 2 and 3. Area 1 is defined from the time when the sample starts to melt at T_l to the time when the temperature starts to be constant. Area 2 is defined at the whole time when the temperature is constant. And area 3 is defined from the time when the temperature

starts to decrease from the constant temperature to the time when the temperature reach T_l again. The correction factor, f, is calculated from the ratio of the average diffusivity of area 2, defined as D_2, and the total average diffusivity of area 1, 2 and 3, defined as D_{1+2+3}. The calculation is summarized in the Eq. (3-7), Eq. (3-8) and Eq. (3-9) below.

$$D_{1+2+3} = \frac{1}{t_4 - t_1} \int_{t_1}^{t_4} D(T,t)dt \qquad (3\text{-}3)$$

$$D_2 = \frac{1}{t_3 - t_2} \int_{t_2}^{t_3} D(T,t)dt \qquad (3\text{-}4)$$

$$f = \frac{D_2}{D_{1+2+3}} \qquad (3\text{-}5)$$

The diffusivity at the annealing temperature is then calculated as

$$D_{anneal} = fD_{meas} \qquad (3\text{-}6)$$

where D_{meas} is the diffusivity measured from the experiment which is calculated from T_l to T_l (Eq.).

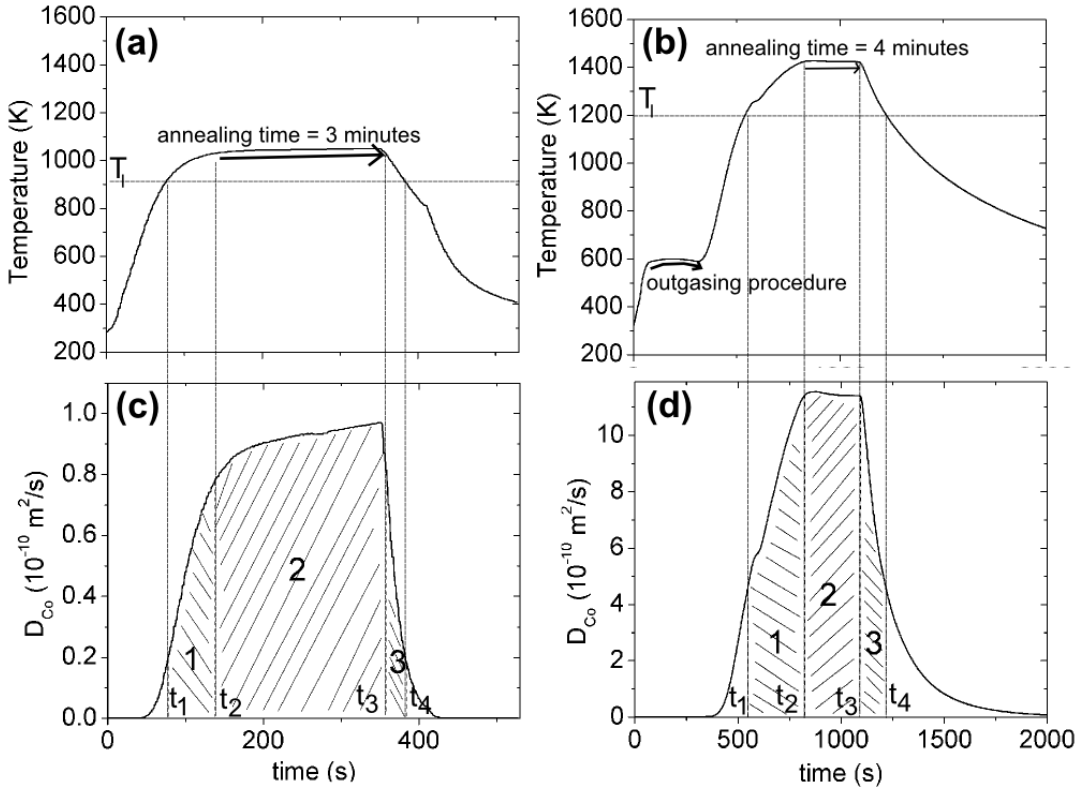

Figure 3-7 (a) Typical annealing profile in Part I, (b) typical annealing profile in Part II, (c) and (d) are the respective diffusivity profile calculated using Arrhenius equation

3.8 Measurement error

In measurement system analysis, there are two sources of measurement error, i.e. systematic error and statistical error. Systematic error originates from the method of analysis being used. It may be reduced by improving the method of the analysis, and is normally expressed as the bias of the measurement. While the statistical error is a random error. It is normally hard to be avoided, but it does not influence the average value of the result, and only broadens the measurement noise. It is a measure of how much the result can produce the same value when the measurement with the same method is repeated several times by different operators or by different time of measurement. Statistical error is normally expressed as repeatability and reproducibility of the measurement.

As radiotracer diffusion is a function of annealing time, penetration depth and annealing temperature, all there variables can contribute to the total error of diffusion measurement, such that

$$D = f(t, x, T) \qquad (3\text{-}7)$$

$$\Delta D = \frac{\partial f}{\partial t}\Delta t + \frac{\partial f}{\partial x}\Delta x + \frac{\partial f}{\partial T}\Delta T \qquad (3\text{-}8)$$

The overall list of the sources of measurement error in this investigation is summarized in Ishikawa diagram in Figure 3-8.

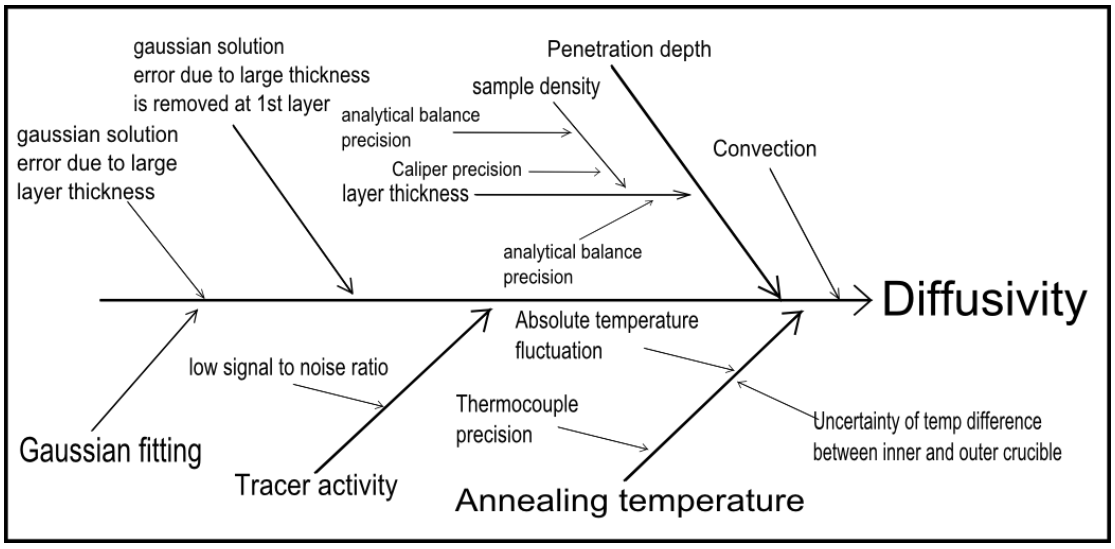

Figure 3-8 Ishikawa diagram showing all sources of errors which can contribute to the measurement error in the determination of diffusion coefficient using radiotracer technique.

Among variables mentioned in Eq. (3-7) and (3-8) above, temperature gives the biggest error contribution in this measurement. And as the dependency of the diffusivity to the temperature is normally less at higher temperature, measuring at high temperature will also reduced the error contribution. As an example, the error contribution of the temperature in vitreloy 4 is about 20 % which arises from the precision of the thermocouple, the standard deviation of the absolute temperature, and the uncertainty of the temperature difference between the inner and outer crucible. In

ternary Zr-Ni-Al system in which the measurement is done at about 200 K more than the measured temperature is vitreloy 4, the error contribution from temperature is less, only 10 %. The second largest error contribution is from the measurement of radiotracer activity which is about 7 %. This is because the very low activity of the tracers was counted not long enough due to time efficiency. Next contribution is error from thin film solution of Fick's second law (Eq. (2-15) and Eq. (2-16)) fitting which is about 5%. Error from the measurement of penetration depth does not contribute very significantly, although the magnitude depends on the geometry of the sample. Sample with much larger diameter than the diffusion length will have larger error contribution of the error than sample with diameter is similar to the diffusion length. As an example, the error contribution from this source in vitreloy 4 which was measured with sample diameter of 8 mm and diffusion length of only about 200 μm is 0.11%. In ternary Zr-Ni-Al system in which the sample geometry is 1.5 mm and diffusion length of about 1 mm has only 0.06% error contribution from this source. The other contribution which can cause error in Gaussian solution of Fick's second law listed in Figure 3-8 is the error which was proposed by Haessner [59]. The initial layer that is allowed to be excluded from diffusion calculation must be less than $0.3\sqrt{Dt}$, in order to get error of less than 1 %. In addition, one should pay attention on the thickness of each layer which should not be more than $0.2\sqrt{Dt}$ so that the systematic error is less than 1%. In all diffusion measurement in this investigation, this is only about 1 - 2 %. By summing up all the error contribution from the sources mentioned above, the systematic error in diffusivity measurement in Vit. 4 is about 20 %, and in binary and ternary Zr-Ni(-Al) systems is about 15 %.

3.9.1 Simultaneous diffusion measurement

The systematic error mentioned above will only be relevant when comparing measurements which are done individually. For example in this investigation, the aim of the investigation is to compare the diffusivity of ^{57}Co and ^{95}Zr in the melt of a

sample. If the measurement of both diffusivities is carried out individually, this systematic error should be considered. However, if the measurement of both diffusivities is carried out simultaneously, this systematic error will be excluded. Only the relative error of both diffusivities, which arises from the fitting of Fick's second law, will be considered. As mentioned, this error is only less than 5 %. In *Part I* of this investigation, diffusivity of ^{57}Co and of ^{95}Zr were measured both individually and simultaneously. While in *Part II*, they all were measured simultaneously.

3.9.2 Error due to convection

Another error contribution which should be considered here is convective flow. Diffusion measurement in simple binary melt is very sensitive to convective flow because of the very low viscosity. Convective flow is massive mobility of particles in a liquid originated from density differences (buoyancy) and surface tension differences due temperature difference, compositional changes or free surfaces (marangoni). In simple binary liquid, the present of free surface can lead the increase in diffusivity measurement up to factor 2, while radial temperature gradient in the absence of free surface can lead the increase of diffusivity up to 50% [53]. For simple binary and ternary melts, measurement using long capillary graphite crucible (see Figure 3-2b) can suppressed the effect of convective flow. In multicomponent Vit. 4 melts, the effect of convective flow is not very significant due to the very viscous nature of the melts at the investigation temperatures.

The experimental set up of these radiotracer diffusion measurement does not allow us to know how large the contribution of convective flow to the measurement result is. However, as QNS probes dynamics on significantly shorter times, its data is not affected by convection [9, 60]. Diffusivity from QNS data also probes the diffusivity of Ni because the signal of the scattering function in Zr-Ni-based melts is dominated by the incoherent scattering from *Ni* [9-10]. And as *Co* and *Ni* have similar chemical characteristics, their diffusivities are expected to be similar [43].

Therefore, when Co radiotracer diffusivity is the same as Ni self-diffusivity from QNS data, it means the radiotracer diffusion measurement is not affected by convective flow.

Chapter 4 Results and discussion

As mentioned in the introduction, the present investigation is divided into two parts. *Part I* is meant to check the general validity of the previous investigation on multicomponent Pd-based glass forming melts [17] on the multicomponent Zr-based glass forming melts. This was done by measuring ^{57}Co and ^{95}Zr radiotracer diffusivities in multicomponent $Zr_{46.75}Ti_{8.25}Cu_{7.5}Ni_{10}Be_{27.5}$ (Vit. 4) above its T_l. This part has been published in Physical Review Letters, thus only a short summary of the results and discussion will be given here.

Part II is meant to understand the behaviour of the Ni and Zr diffusivities in multicomponent Vit. 4 melt by measuring ^{57}Co and ^{95}Zr radiotracer diffusivities in simpler Zr-based system melts in the same way as it was done in the first part. The effects of packing density and chemical short range order (CSRO) on the atomic diffusion in these melts will also be discussed. As the publication of this results is still under preparation, the full version of results and discussion will be given here.

4.1 Part I: Diffusion in multicomponent Zr-based glass forming melt

As mentioned earlier, the result of this part has been published, thus only a brief summary will be given here. The publication can be seen in Appendix A, and the details of experimental results, which is not shown in the publication, can be seen in Appendix B.

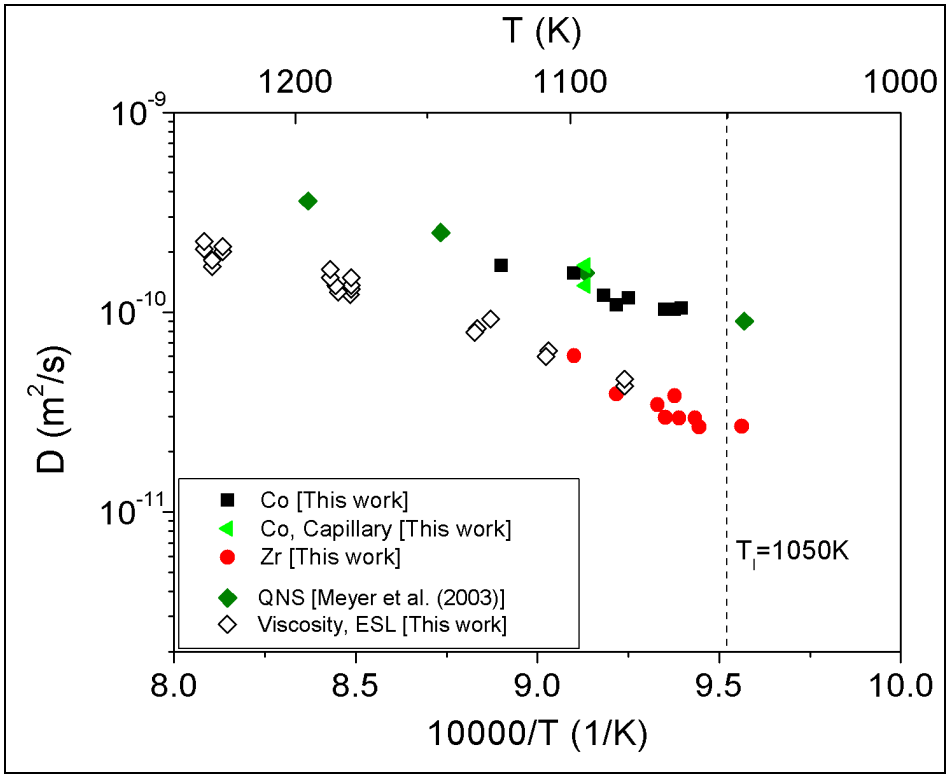

Figure 4-1 Arrhenius plot of diffusion in Vit. 4 in equilibrium melt. The ^{57}Co and ^{95}Zr diffusivities, including data points obtained from measurement with long capillary technique (green triangles), are presented together with diffusivities from QNS [9]. Diffusivities calculated via Stokes-Einstein relation from viscosity data measured using electrostatic levitation technique by DLR [7] are also shown. It was calculated using the covalent radius of 145 pm, which is the radius of Zr atoms.

In Pd-based glass forming melts, it has been shown that there was no component diffusion decoupling between the larger component Pd and the smaller components above T_c of MCT and it was in agreement with MCT prediction [17]. In contrast to this result, in the present investigation in Zr-based, $Zr_{46.75}Ti_{8.25}Cu_{7.5}Ni_{10}Be_{27.5}$ (Vit. 4), glass forming melt, the measurement of ^{57}Co and ^{95}Zr radiotracer diffusivities has shown a significant decoupling of Zr diffusivities from the diffusivities of the smaller components as large as a factor of four at T_l (see Figure 4-1). As shown also in Figure 4-1, even though the Zr diffusivities decouple from the diffusivities of the smaller components, the SE relation (see Eq. (2-2)) is well obeyed for the larger component Zr. This result is the same as it has been reported earlier for larger component Pd in the multicomponent Pd-based glass forming systems below T_c. This finding was interpreted as the existence of a slow subsystem made up by the large atoms that have to rearrange for structural relaxation and viscous flow [17].

Therefore, according to the previous result interpretation in Pd-based melt, the present investigation shows that the slow subsystem formed by the large atom Zr is still preserved in the stable molten state above T_c of MCT and even above T_l. In other words, the gradual decay of the energy barriers for diffusion of Zr, which should have set in at T_c as it has been observed in Pd-based systems [17], extends to higher temperatures at least 150 K above T_l of Vit. 4. From energy landscape point of view [31, 38], the present result shows that in the melt, Zr atoms may still form stronger temporary bonding with the nearest neighbours compared to the other atoms. Thus, this bonding has to be broken by thermal activation energy and slows down the diffusion of the Zr atoms.

4.2 Part II: Diffusion in the melt of simple Zr-based glass forming systems

The publication of the present part is still under preparation when this dissertation is prepared. Therefore, as mentioned before, a complete version of result and discussion is given. This section is divided into two subsections. The First is the experimental results in which the measurement artefacts are also explained. The second section is the discussion part. In particular, the origin of the component diffusion decoupling between Ni and Zr diffusivities in multicomponent Vit.4 melt (from Part I of this investigation) will be explained by the results of the present part (Part II). In addition, the influence of packing density and chemical short range order on the component diffusion decoupling.

4.2.1 Results

- **Diffusion profiles**

Before the results are discussed here, it is worth explaining the difference between penetration profiles and diffusion profiles which are normally used in radiotracer diffusion experiments. Penetration profiles are all data points which were obtained from the experiments regardless of whether they are affected by measurement artefacts. Diffusion profiles are those data points which can be attributed to diffusion processes. It can be checked from how good the data points can be fitted using Fick's second law in Eq. (2-16), and how consistent the results are, which are obtained from several measurements done at the same temperature and different annealing time, and also obtained from different diffusion measurement methods. For instance, in the present investigation, it can be checked by comparing the results of ^{57}Co tracer diffusion measurement with the Ni self-diffusivity data obtained from QNS.

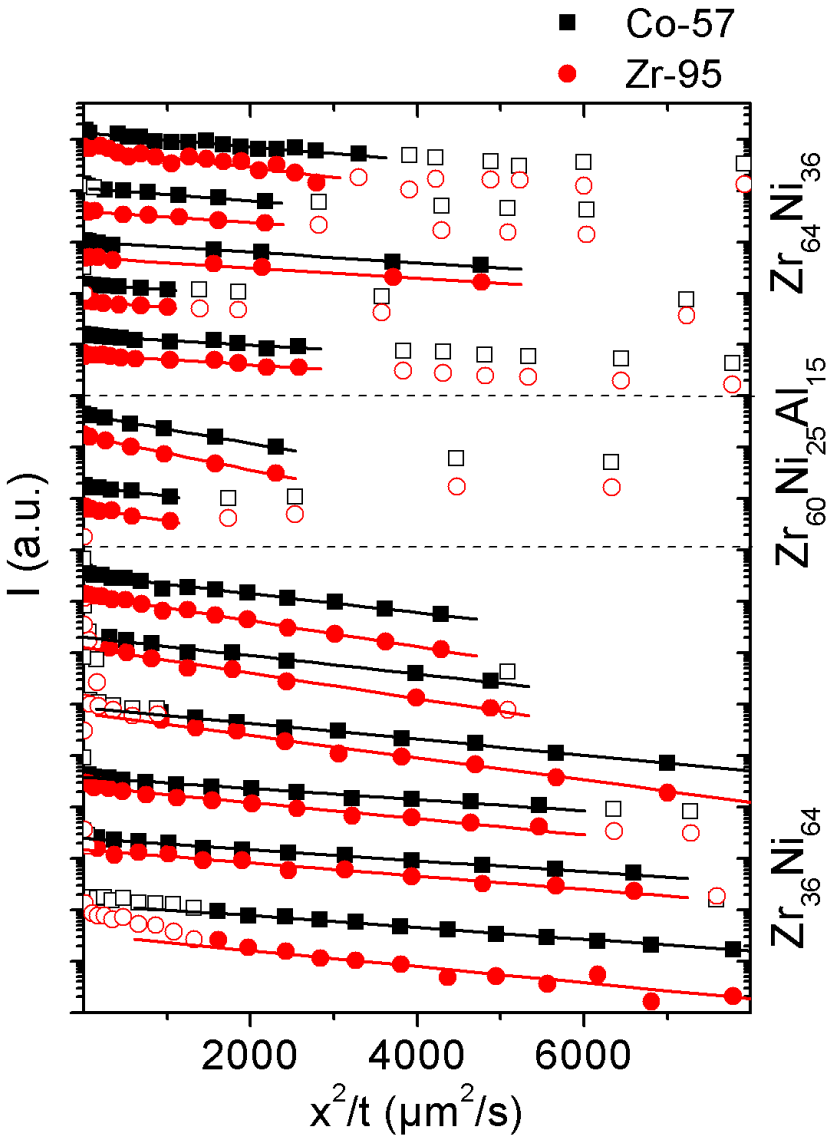

Figure 4-2 ^{57}Co **and** ^{95}Zr **penetration profiles from simultaneous diffusion experiments in equilibrium melt of** $Zr_{64}Ni_{36}$, $Zr_{60}Ni_{25}Al_{15}$ **and** $Zr_{36}Ni_{64}$. **The activity of** ^{57}Co **and** ^{95}Zr **is plotted on logarithmic scale vs. the square of the penetration depth divided by the annealing time. The profiles of** $Zr_{64}Ni_{36}$ **from top to bottom are shown at temperatures 1304** K, **1388** K, **1388** K, **1438** K **and 1438** K, **sequentially. The profiles of** $Zr_{60}Ni_{25}Al_{15}$ **from top to bottom are shown at temperatures 1290** K **and 1388** K, **sequentially. And the profiles of** $Zr_{36}Ni_{64}$ **from top to bottom are shown at temperatures 1388** K, **1388** K, **1388** K, **1428** K, **1469** K, **1469** K **and 1488** K, **sequentially. The full symbols are the long range diffusion profile, whereas the open symbols are affected by experimental artefacts and are not taken into account for evaluation.**

The ^{57}Co and ^{95}Zr penetration profiles of the present investigations, which are obtained from simultaneous diffusion experiments in equilibrium melt of $Zr_{64}Ni_{36}$, $Zr_{60}Ni_{25}Al_{15}$ and $Zr_{36}Ni_{64}$ can be seen in Figure 4-3. The detail of the measurement results can be found in Appendix B. In Figure 4-3, the diffusion profiles are marked as full symbols and are fitted with Fick's second law which is shown as the linear lines. The data points, which are considered to be affected by measurement artefacts, are marked as empty symbols.

As seen also in this figure, the diffusion profiles in the melts of $Zr_{64}Ni_{36}$ and $Zr_{60}Ni_{25}Al_{15}$ are much shorter than those in $Zr_{36}Ni_{64}$ melt. In order to clearly see the difference between the diffusion profiles and the penetration profiles which may be affected by measurement artefacts, the intensity in linear scale from one of the penetration profiles from $Zr_{36}Ni_{64}$ (black circles) and from $Zr_{60}Ni_{25}Al_{15}$ (red squares) are plotted against the penetration depth (also in linear scale) as seen in Figure 4-3. In this figure, the Gaussian distribution fit is also drawn for each set of penetration profiles and presented as solid lines. As seen in this figure, almost all data points from $Zr_{36}Ni_{64}$ fit to one single Gaussian distribution, while in $Zr_{60}Ni_{25}Al_{15}$, not all data points fit to one single Gaussian distribution. Additionally, the calculations of diffusivity from data points which fit to the Gaussian distribution are the same as diffusivities from QNS. This is the basis on how the diffusion profiles are chosen, and it suggests that those data points, which are outside the Gaussian fit, might be affected by some processes which occur in the molten state and can provide fast diffusion paths for the tracers, e.g. bubbles. However, using the current methods, these processes could not be investigated, unless diffusion annealing was done in a furnace integrated with a radiographer instrument which may be able to observe those processes [53].

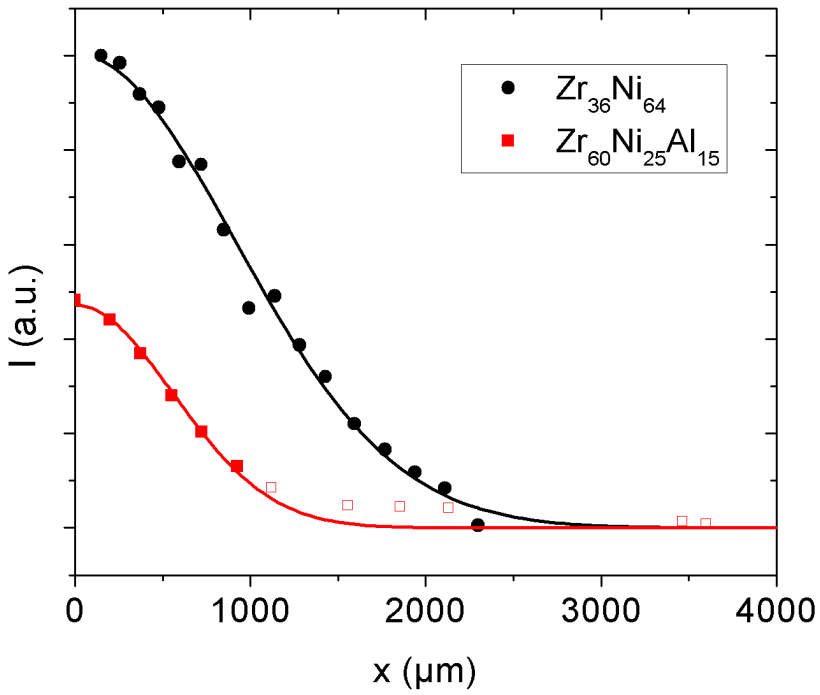

Figure 4-3 Penetration profiles showing intensity versus the penetration depth, both are in linear scale. It shows penetration profiles and the Gaussian fit of $Zr_{36}Ni_{64}$ melt (black circle) at annealing temperature and time 1388 K and 1038 s, respectively, and of $Zr_{60}Ni_{25}Al_{15}$ melt (red square) at annealing temperature and time at 1290 K and 542 s, respectively.

- **Arrhenius plot**

The temperature dependence of diffusion is frequently shown in Arrhenius plot. In Arrhenius plot the logarithm of diffusivity is plotted versus the reciprocal of absolute temperature. The Arrhenius plot, as shown in Figure 4-4, shows the diffusivities of ^{57}Co and ^{95}Zr in the melt of $Zr_{64}Ni_{36}$ (Figure 4-4a), $Zr_{60}Ni_{25}Al_{15}$ (Figure 4-4b) and $Zr_{36}Ni_{64}$ (Figure 4-4c). This figure also depicts the results from QNS which represent diffusivities of Ni. As seen in this figure, the present ^{57}Co diffusivities in those three systems are in agreement with diffusivities from QNS, thus the effects of convective flow are ruled out.

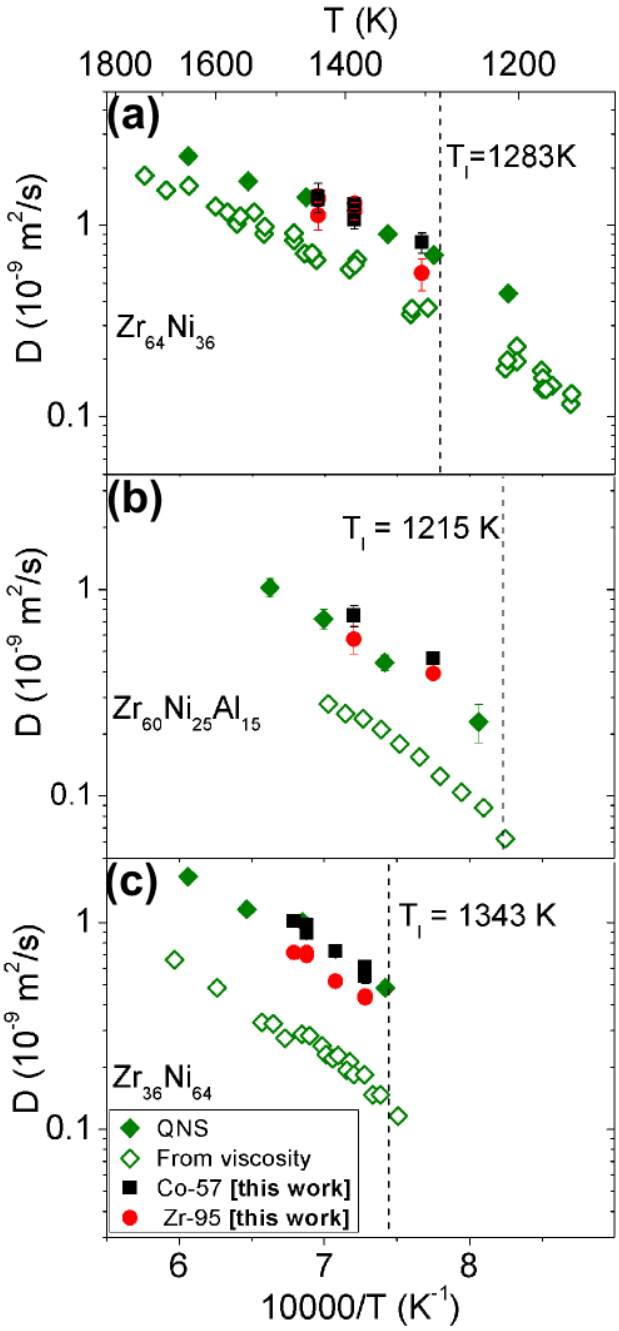

Figure 4-4 Arrhenius plot of diffusion in equilibrium melt of $Zr_{64}Ni_{36}$, $Zr_{60}Ni_{25}Al_{15}$ and $Zr_{36}Ni_{64}$. The ^{57}Co and ^{95}Zr diffusivities are presented together with diffusivities from QNS of each system [10]. Diffusivities calculated via Stokes-Einstein relation from viscosity data, measured using electrostatic levitation technique by DLR (viscosity data of $Zr_{64}Ni_{36}$ is referred to Brillo et. al [47]) are also shown. It was calculated using the covalent radius of 145 pm, which is the covalent radius of Zr atom [50].

The diffusivities calculated from the measured viscosity (see section 2.4.2) via SE-relation according to Eq. (2-2) in the melt of $Zr_{64}Ni_{36}$, $Zr_{60}Ni_{25}Al_{15}$ and $Zr_{36}Ni_{64}$ systems are also presented in Figure 4-4 as empty diamonds. Although it seems that the calculated diffusivities from viscosity data differ from the measured diffusivities, their differences are only about a factor of two, and they follow the similar temperature dependency. In addition, the diffusivities and the viscosity values were obtained from two independent measurements, thus, the factor of two differences may come from the systematic error of the two independent measurements.

4.2.2 Discussion

In order to see clearly the component diffusion decoupling, the ratio of the diffusivity values of Co and Zr (decoupling factor) is calculated. The resulting decoupling factors are then compared with ratio of the square root of the reciprocal masses, $\sqrt{\frac{m_{Zr-95}}{m_{Co-57}}}$, as well as the ratio of the reciprocal radius of the atoms, $\frac{r_{Zr}}{r_{Co}}$, to show the mass and size effects, respectively. The resulting component diffusion decoupling factor, as well as the ratio of the square root of the reciprocal masses and the ratio of the reciprocal radius, in $Zr_{64}Ni_{36}$, $Zr_{60}Ni_{25}Al_{15}$ and $Zr_{36}Ni_{64}$ melts are presented in Figure 4-5. This figure shows, in all of those three systems, that Co diffusivities differ from Zr diffusivities only by factor less than 2. This results are still within the range of mass effects and size effects, and are similar to the characteristic of simple metallic melts in equilibrium, as mentioned in Section 2.3.1. However, this result is in contrast to the previous investigation on multicomponent Vit. 4 melt, in which the component diffusivities are significantly decoupled, as large as a factor 4 at T_l.

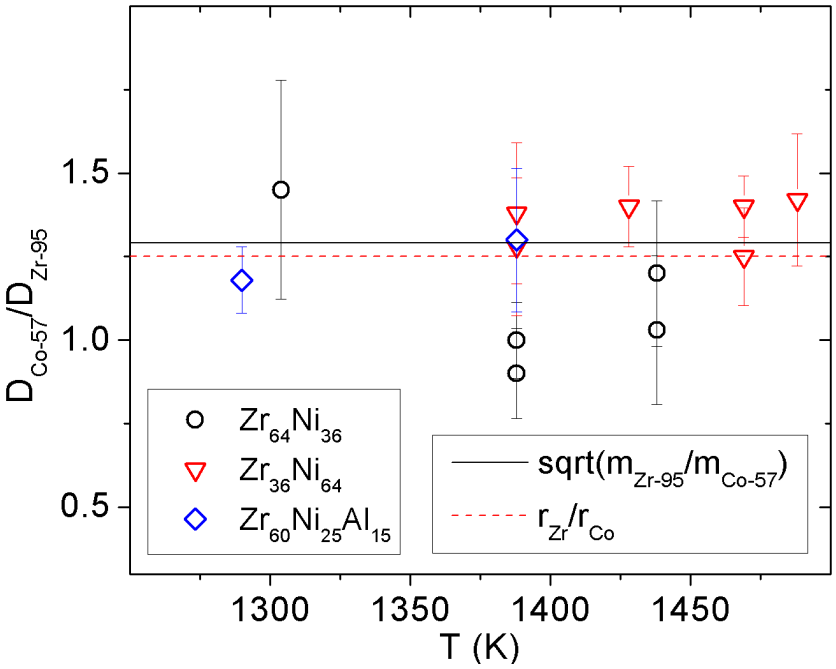

Figure 4-5 Component diffusivities decoupling of ^{57}Co and ^{95}Zr diffusivities in equilibrium melt of $Zr_{64}Ni_{36}$, $Zr_{60}Ni_{25}Al_{15}$ and $Zr_{36}Ni_{64}$. The error bar shown has 95% confidence interval. The square root of ^{95}Zr mass to ^{57}Co mass ratio and the Co radius to Zr radius ratio are also given as a solid and dash lines, respectively.

As mentioned earlier in Section 2.4.2, Ni-self-diffusivities measured by QNS in binary Zr-rich $Zr_{64}Ni_{36}$ have shown similar values as Ni-self-diffusivities in multicomponent Vit. 4 [10]. And it is only their liquidus temperatures, T_l, which are different. Therefore, the binary Zr-rich $Zr_{64}Ni_{36}$ system can be used as a simpler model to understand the diffusion in the multicomponent Vit. 4. In Figure 4-6, the Ni-self-diffusivities from QNS in equilibrium melt of $Zr_{64}Ni_{36}$ and Vit.4 are again shown together with their ^{57}Co and ^{95}Zr diffusivities obtained from the present investigations. If the diffusivities of ^{57}Co and ^{95}Zr in Vit. 4, which are decoupled by factor 4 at its T_l, in this figure are extrapolated to higher temperatures, the decoupling decreases into a factor of less than two at around 1280 K, similar to the decoupling

factor of ^{57}Co and ^{95}Zr diffusivities in $Zr_{64}Ni_{36}$ at its respective T_l. Therefore, these results are implicitly consistent with the results reported in Part I. Within the notion of energy landscape and atomic connectivity network theory [31, 38], one may interpret that at low temperature near the T_l of Vit. 4, the bonds of Zr atoms with the nearest neighbours are significant and stronger than the bonds of the Ni atoms. Consequently, additional thermal activation energy is needed to break the bonds and the Zr atoms are slowed down. As the temperature increases, the diffusion barriers decay gradually, and as the temperature reaches above the T_l of $Zr_{64}Ni_{36}$, the Zr diffusion is not anymore in energy landscape controlled regime, thus Zr and Ni diffuse almost equally.

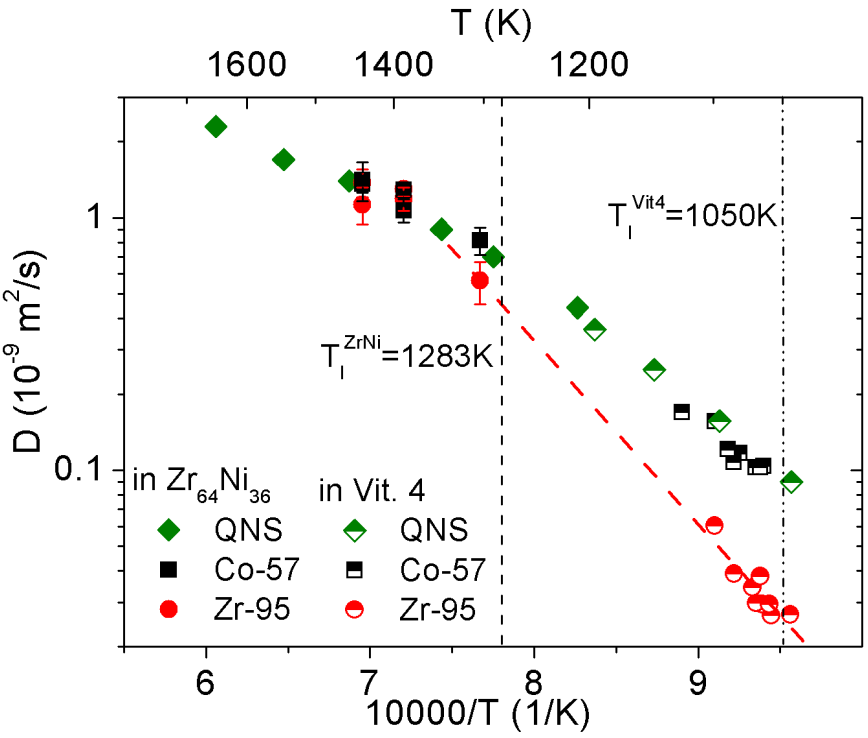

Figure 4-6 ^{57}Co and ^{95}Zr diffusivities in equilibrium melt of $Zr_{64}Ni_{36}$ are presented together with ^{57}Co and ^{95}Zr diffusivities in equilibrium melt of Vit. 4. The Ni-self-diffusivities from QNS data of both $Zr_{64}Ni_{36}$ (full symbols) and Vit. 4 melts (half-full symbols) are also shown.

It has been also reported that diffusion in dense metallic melts is similar to diffusion in hard sphere systems, in which the diffusion is determined only by the packing density [14]. Systems with higher packing density tend to have sluggish (or slow) diffusion compared to systems with lower packing density [8, 14]. If we assumed that the packing density is independent of the alloy composition, molar volume, V_m, can be used to qualitatively describe the packing density of the system (see Section 2.4.2).

Now let us see again Figure 4-5. Although the component diffusion decoupling in the melt of those three simpler systems is still within the range of size and mass effects, one can still see a tendency that the decoupling factor increases sequentially from $Zr_{64}Ni_{36}$ to $Zr_{60}Ni_{25}Al_{15}$ and $Zr_{36}Ni_{64}$ melts. Furthermore, the three melts show different packing density as explained in Section 2.4.2. Therefore, one may try to understand how packing density influences the atomic diffusion and the component diffusion decoupling in these three melts. This can be done by comparing the diffusion and the decoupling factor of the respective melts with their respective molar volume as seen in Figure 4-7

In Figure 4-7a, the Co and Zr diffusivities at the same factor above the respective T_l of the respective alloy are presented as a function of the respective molar volume, V_m of the melts. Large V_m means low packing density. As shown in these figures, packing density increases sequentially from $Zr_{64}Ni_{36}$ to $Zr_{60}Ni_{25}Al_{15}$ and $Zr_{36}Ni_{64}$. However, the diffusivity increases sequentially from $Zr_{60}Ni_{25}Al_{15}$ to $Zr_{36}Ni_{64}$ and $Zr_{64}Ni_{36}$. Thus, there is no direct correlation between diffusivities and packing density in the three melts. The diffusion in binary Zr-Ni melts can be understood by the influence of the packing density. However the slow diffusion in $Zr_{60}Ni_{25}Al_{15}$, compared to the binary Zr-Ni melts, may be related to the presence of CSRO around the Al atoms in its structure (see section 2.4.2).

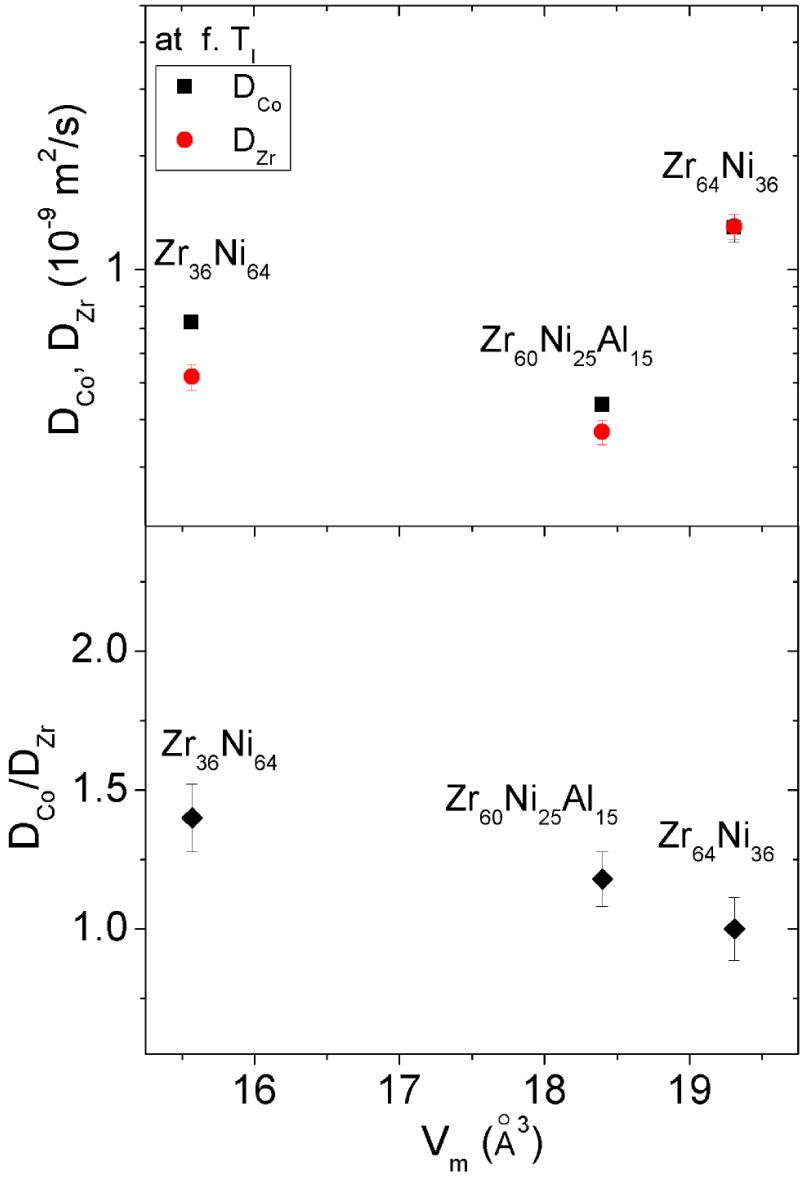

Figure 4-7 Comparison of (a) *Co* and *Zr* diffusivities in logarithmic scale and (b) decoupling factor D_{Co}/D_{Zr} with respect to the molar volume V_m of $Zr_{64}Ni_{36}$, $Zr_{60}Ni_{25}Al_{15}$ and $Zr_{36}Ni_{64}$ at 1388 K, 1290 K and 1428 K, respectively. These temperatures have the same factor above their respective T_l.

In Figure 4-7b, the decoupling factors at the same factor above the respective T_l of the alloys are also presented as a function of the respective V_m of the melts. As shown in this figure, the component diffusion decoupling increases as the packing density increases. Therefore, results directly show the influence of packing density on the component diffusion decoupling.

As mentioned also in section 2.4.2, the recent MCT studies on the hard-sphere model of $Zr_{64}Ni_{36}$ melt, have shown that the diffusivities of Ni differ from the diffusivities of Zr by a factor of two [16]. Hard-sphere model is a system which considers only packing density but no CSRO. However, the MCT studies on the real system of $Zr_{64}Ni_{36}$ melt have shown that diffusivities of Ni and Zr are the same [16]. The melt of $Zr_{64}Ni_{36}$ has been reported to show an evidence of CSRO in its structure [48]. The striking observation here is that the present experimental results for the melt of $Zr_{64}Ni_{36}$ (see Figure 4-4a) are in good agreement with the above mentioned MCT studies, in which diffusivities of Co are found to be the same as diffusivities of Zr. Therefore, the present results are the first experimental evidence which shows the effect of CSRO on the reduction of component diffusion decoupling. The results of $Zr_{36}Ni_{64}$ melt, however, are contradicted to the MCT studies mentioned above. The component diffusion decoupling in $Zr_{36}Ni_{64}$ melt is about a factor of 1.4±0.16 at all investigation temperatures. This results are in agreement with molecular dynamic simulation on deeply quenched $Zr_{50}Ni_{50}$ [13]. It can be assumed that it is because the effect of packing density in $Zr_{36}Ni_{64}$ melt is so dominant that the effect of CSRO on the component diffusion decoupling becomes minor.

Chapter 5 Conclusion and Outlook

According to mode coupling theory (MCT) and Stokes-Einstein (SE) relation, all components of a simple metallic system should have the same diffusivities in its equilibrium melt. The previous experimental results on multicomponent Pd-based systems have shown a good agreement with these theories [17]. In Pd-based systems, it has been reported that all components diffuse almost equally at temperatures above its liquidus temperature, T_l. Diffusivities of the larger component Pd started to significantly decouple from the diffusivities of the smaller components by many order of magnitude when the melts were cooled down below the critical temperature, T_c, of MCT, slightly below T_l. It was because atoms must overcome high energy barriers for diffusion. The large component Pd, however, obeyed SE relation in the whole range of temperatures; from the stable melt down to the glass transition temperature.

In order to check whether these results are also generally accepted for another class of metallic glass formers, e.g. Zr-based glass formers, simultaneous radiotracer ^{57}Co and ^{95}Zr diffusion experiments were performed in two parts. In Part I, the experiments were performed on the melt of multicomponent Zr-based system, $Zr_{46.75}Ti_{8.25}Cu_{7.5}Ni_{10}Be_{27.5}$ (Vitreloy 4). While, in Part II, the experiments were done on simpler Zr-based systems, $Zr_{64}Ni_{36}$, $Zr_{36}Ni_{64}$ and $Zr_{60}Ni_{25}Al_{15}$ above their respective T_l were done. In the end of this work, the effects of component complexity of the system on the atomic diffusion in the melt could be understood. Additionally from the experimental results of the simpler systems, it is expected that the atomic diffusion in multicomponent Zr-based melts could be explained. The effects of packing density and chemical short range order (CSRO) on the atomic diffusion in the melt can be explained as well.

The experimental results of Part I on multicomponent Vit. 4 melt have shown that Zr diffusion differed significantly from the diffusion of the smaller components by a factor of 4 at its T_l, although it obeyed SE relation. The difference between the diffusivities of the large and the smaller atoms is called component diffusion decoupling. On the other hand, the experimental results of Part II on the melt of simpler systems, which have T_l of about 150 K higher than T_l of Vit. 4, have shown that component diffusion decoupling was not very significant. It was only a factor of less than two, and was similar to the component diffusion decoupling in simpler metallic and in Pd-based melts. These results suggested that, the slow subsystem formed by the large component Zr was still preserved even in the melt of the multicomponent Vit. 4 which has T_l about 150 K lower than the T_l of the simpler Zr-based systems. In other words, in this temperature regime, Zr atoms were still in energy landscape influenced regime, and still formed stronger bonds with the nearest neighbours compared to the smaller atoms. Thus, these bonds had to be broken by thermal activation energy and the diffusion of Zr atoms were slowed down.

In order to see the effect of packing density on the diffusion in the simpler melts in Part II, the diffusivities in the simpler melts were plotted with the respective packing density of the melts at temperature with the same factor above the respective T_l. The results have shown that only the diffusivities in the binary Zr-based melts showed direct correlation with the packing density. The packing density of $Zr_{36}Ni_{64}$ melt is lower than that of $Zr_{64}Ni_{36}$ melt, thus the diffusion in $Zr_{36}Ni_{64}$ melt was slower than the diffusion in $Zr_{64}Ni_{36}$ melt. However, the diffusion in $Zr_{60}Ni_{25}Al_{15}$ melt is the slowest although its packing density is in between the packing density of $Zr_{36}Ni_{64}$ and $Zr_{64}Ni_{36}$ melts. This could be assumed that the slow diffusion in $Zr_{60}Ni_{25}Al_{15}$ melt was related to the CSRO around the Al atoms.

Furthermore, although the experimental results of the $Zr_{64}Ni_{36}$, $Zr_{36}Ni_{64}$ and $Zr_{60}Ni_{25}Al_{15}$ melts have shown that their component diffusion decoupling was similar to the component diffusion decoupling in simple metallic melts, it was observed that

the decoupling increased sequentially from $Zr_{64}Ni_{36}$ to $Zr_{60}Ni_{25}Al_{15}$ and $Zr_{36}Ni_{64}$. These results suggested that the component diffusion decoupling was mainly influenced by packing density. In addition, the component diffusion decoupling in $Zr_{64}Ni_{36}$ melt was in agreement with the MCT studies on the same system . Therefore, these results have also implicitly shown the influence of CSRO in reducing the component diffusion decoupling. However, the results on $Zr_{36}Ni_{64}$ were contradicted to the above mentioned MCT studies where diffusivities of Co and Zr were decoupled with a factor of about 1.4 ± 0.16. It could be assumed it was because the packing density in $Zr_{36}Ni_{64}$ melt was so dominant that the effect of CSRO on the component diffusion decoupling became minor. In fact, how the CSRO effect influences the component diffusion decoupling still remains open. For instance, component diffusion decoupling has also been reported on deeply quenched $Zr_{50}Ni_{50}$ [13] and on Ni-rich Al-Ni melts [15]. Therefore, similar MCT studies on the $Zr_{36}Ni_{64}$ melt, as have been done on $Zr_{36}Ni_{64}$ melt would be worth performing to further support the findings.

Acknowledgement

I would like to express my greatest gratitude to **Prof. Dr. Klaus Rätzke** who has been a great supervisor for me. He has taught me theories and experimental methods, shared his experiences and continuously encouraged me during the completion of this work. I would also like to express my deepest thank to **Prof. Dr. Franz Faupel** who has given me chance to become his student and to use the laboratory and working spaces in his working group.

In addition, I gratefully acknowledge the financial support from *Deutsche Forschungsgemeinschaft* (DFG), and the irradiation of the Zr tracers by **Gregor Bukalis** from Helmholtz Zentrum Berlin. I would also like to express my gratitude to **Prof. Dr. Andreas Meyer**, **Dr.-Ing. Fan Yang** and **Pascal Heintzmann** from DLR in Cologne who has shared their experiences and provided samples, as well as provided time for scientific discussion related to this project. A thank you also to **Dr.-Ing. Alexander Bartsch**, who has explained me the details about the experimental techniques at the beginning of this work.

The completion of this work will never happen without the technical support from **Stefan Rehders** on building the furnace. Therefore, a great thank you to him. The technical support from **Christoph Ochmann**, **Reiner Kloth** and **Peter Sommer** is also greatly acknowledged. I would also like to thank to my colleagues: **Christian Ohrt** and **Tönjes Koschine**, who have helped me and assisted me in the laboratory when I was working with radioactive tracers. A special thank to **Elisabeth Gill** who has assisted and completed part of this work for her master thesis. A great thank you to **Sebastian Zabel** for the great discussion, suggestion and correction of the thesis.

Last but not least, I am very truly grateful to my husband, **Tilo Peter** for his support and continuous love. This thesis will never been completed without his patient and understanding.

Bibliography

[1] S. Schneider, J Phys-Condens Mat **13**, 7723 (2001).
[2] J. Schroers, Phys Today **66**, 32 (2013).
[3] A. Inoue, and N. Nishiyama, Mrs Bull **32**, 651 (2007).
[4] J. Schroers *et al.*, Mat Sci Eng a-Struct **449**, 235 (2007).
[5] R. C. Sekol *et al.*, Small **9**, 2081 (2013).
[6] G. Kumar, A. Desai, and J. Schroers, Adv Mater **23**, 461 (2011).
[7] F. Yang, T. Unruh, and A. Meyer, Epl-Europhys Lett **107** (2014).
[8] F. Yang *et al.*, Epl-Europhys Lett **107** (2014).
[9] A. Meyer *et al.*, Appl Phys Lett **83**, 3894 (2003).
[10] D. Holland-Moritz *et al.*, Journal of Physics **144** (2009).
[11] X. J. Han, and H. R. Schober, Phys Rev B **83** (2011).
[12] P. Kuhn *et al.*, Phys Rev B **90** (2014).
[13] H. Teichler, J Non-Cryst Solids **293**, 339 (2001).
[14] S. M. Chathoth *et al.*, Appl Phys Lett **85**, 4881 (2004).
[15] S. K. Das *et al.*, Appl Phys Lett **86** (2005).
[16] T. Voigtmann *et al.*, Epl-Europhys Lett **82** (2008).
[17] A. Bartsch *et al.*, Physical Review Letters **104** (2010).
[18] J. F. Loffler, Intermetallics **11**, 979 (2003).
[19] H. Mehrer, *Diffusion in Solids: Fundamentals, Methods, Materials, Diffusion-Controlled Processes* (Springer-Verlag Berlin Heidelberg, Berlin Heiderberg New York, 2007).
[20] R. W. Cahn, P. Haasen, and A. Kramer, in *Materials Science and Technology*, edited by J. Zarzycki (VCH Publishers Inc., New York, 1991).
[21] R. Brown, in *A Brief Account of Microscopical Observations*1827), pp. 465
[22] A. Einstein, Annalen der Physik **17**, 549 (1905).
[23] W. Sutherland, Philosophical Magazine and Journal of Science **9**, 781 (1905).
[24] M. Miller, and P. Liaw, *Bulk Metallic Glasses: an Overview* (Springer, USA, 2008).
[25] D. Caprion, J. Matsui, and H. R. Schober, Physical Review Letters **85**, 4293 (2000).
[26] P. Klugkist, K. Ratzke, and F. Faupel, Physical Review Letters **81**, 614 (1998).
[27] A. Heesemann *et al.*, Physical Review Letters **84**, 1467 (2000).
[28] A. Bartsch *et al.*, Appl Phys Lett **89** (2006).
[29] S. K. Kumar, G. Szamel, and J. F. Douglas, J Chem Phys **124** (2006).
[30] J. Brillo, and I. Egry, Int J Thermophys **24**, 1155 (2003).
[31] P. G. Debenedetti, and F. H. Stillinger, Nature **410**, 259 (2001).
[32] F. H. Stillinger, Science **267**, 1935 (1995).
[33] D. R. Reichman, and P. Charbonneau, J Stat Mech-Theory E (2005).
[34] W. Kob, in *Lecture notes for Les Houches 2002 Summer School - Session LXXVII Slow Relaxations and Nonequilibrium Dynamics in Condensed Matter*Montpellier, 2002).
[35] V. Zöllmer, K. Ratzke, and F. Faupel, J Mater Res **18**, 2688 (2003).
[36] A. Griesche *et al.*, J Non-Cryst Solids **336**, 173 (2004).
[37] T. Egami, K. Maeda, and V. Vitek, Philos Mag A **41**, 883 (1980).

[38] T. Iwashita, D. M. Nicholson, and T. Egami, Physical Review Letters **110** (2013).
[39] S. M. Chathoth, in *Physik-Department E13* (Technische Universität München, München, 2005).
[40] K. Georgarakis *et al.*, J Appl Phys **108** (2010).
[41] P. M. Ossi, *Disordered Materials: An Introduction* (Springer-Verlag, Heidelberg, 2006).
[42] J. S. Kirkaldy, and D. J. Young, *Diffusion in The Condensed State* (The Institute of Metals, London, 1987).
[43] P. Klugkist, in *Technische Fakultät* (Christian-Albrecht Universität Kiel, 1999).
[44] W. L. Johnson, Mrs Bull **24**, 42 (1999).
[45] H. Yasuda *et al.*, Mater Trans **46**, 2762 (2005).
[46] A. Meyer *et al.*, Physical Review Letters **80**, 4454 (1998).
[47] J. Brillo, A. I. Pommrich, and A. Meyer, Physical Review Letters **107** (2011).
[48] D. Holland-Moritz *et al.*, Phys Rev B **79** (2009).
[49] M. Guerdane, and H. Teichler, Phys Rev B **65** (2002).
[50] L. Pauling, J Am Chem Soc **69**, 542 (1947).
[51] R. W. Cahn, P. Haasen, and E. J. Kramer, in *Materials Science and Technology: A Comprehensive Treatment*, edited by E. Lifshin (VCH Publishers Inc., New York, 1992).
[52] F. Faupel *et al.*, Rev Mod Phys **75**, 237 (2003).
[53] F. Kargl *et al.*, High Temp-High Press **42**, 3 (2013).
[54] P. Klugkist *et al.*, Phil Mag Lett **79**, 827 (1999).
[55] A. Bartsch, in *Technische Fakultät* (Christian-Albrecht Universität, Kiel, 2009).
[56] M. Ohring, *The Materials Science of Thin Films* (Academic Press, California, 1992).
[57] I. I. Vaisman, and M. L. Berkowitz, J Am Chem Soc **114**, 7889 (1992).
[58] D. R. Lide, *Handbook of Chemistry and Physics* (CRS Press LLC, New York, 2004).
[59] A. Haessner, in *TU Dresden* (TU Dresden, Dresden, 1963).
[60] A. Meyer, Phys Rev B **66** (2002).

Appendix A Publication for diffusion in multi-component Zr-based melt

Decoupling of Component Diffusion in a Glass-Forming $Zr_{46.75}Ti_{8.25}Cu_{7.5}Ni_{10}Be_{27.5}$ Melt Far above the Liquidus Temperature

S. W. Basuki, A. Bartsch, F. Yang, K. Rätzke, A. Meyer, and F. Faupel

PRL **113**, 165901 (2014)

Decoupling of Component Diffusion in a Glass-Forming $Zr_{46.75}Ti_{8.25}Cu_{7.5}Ni_{10}Be_{27.5}$ Melt Far above the Liquidus Temperature

Sri Wahyuni Basuki,[1] Alexander Bartsch,[1] Fan Yang,[2] Klaus Rätzke,[1] Andreas Meyer,[2] and Franz Faupel[1,*]
[1]*Institut für Materialwissenschaft–Lehrstuhl für Materialverbunde, Technische Fakultät, Christian-Albrechts-Universität zu Kiel, Kaiserstrasse 2, D-24143 Kiel, Germany*
[2]*Institut für Materialphysik im Weltraum, Deutsches Zentrum für Luft- und Raumfahrt (DLR) 51170 Köln, Germany*
(Received 24 March 2014; published 13 October 2014)

We report ^{95}Zr and ^{57}Co radiotracer diffusivities and viscosity data in the equilibrium liquid state of a bulk metallic glass forming $Zr_{46.75}Ti_{8.25}Cu_{7.5}Ni_{10}Be_{27.5}$ melt (Vitreloy 4) far above the liquidus temperature T_l that are not affected by convection, as evidenced via quasielastic neutron scattering. Zr diffusion is strongly decoupled from diffusion of the smaller components by more than a factor of 4 at T_l, although it obeys the Stokes-Einstein equation. The results suggest that, in the present Zr-based metallic glass forming systems, diffusion and viscous flow start to develop solidlike, i.e., energy-landscape-controlled, features already in the stable liquid state more than 300 K above the mode coupling temperature T_c.

DOI: 10.1103/PhysRevLett.113.165901 PACS numbers: 66.10.C-, 66.20.Ej

Metallic glasses and particularly the multicomponent bulk metallic glasses are very interesting engineering materials. They are stronger than most steels and can be molded like plastics. In addition, they exhibit intriguing functional properties [1–3]. During recent years, advanced multicomponent glass forming alloys with excellent glass forming ability also received much attention in the glass community as model systems for studying the glass transition, which is currently a very active research topic in physics [4–8]. The attraction of metallic glass formers also for researchers working on ceramic or molecular glasses or on the dynamics of liquids and melts lies in their simple structure being made up of spherical atoms without or with relatively weak directional bonding, rotational degrees of freedom, or side chains, for instance. The glass forming ability of multicomponent metallic glass formers neither arises from strong directed covalent bonding, as in the traditional oxide glasses or amorphous semiconductors, nor does it arise from structural asymmetry, as in single component molecular glass formers, but it is due to dynamic asymmetry which mainly originates from size disparity and short-range order [7,9–11]. Additional thermodynamic aspects [12–14] and the "confusion principle" [15,16] also play a role.

In an ideal liquid at high temperatures, diffusion proceeds via uncorrelated binary collisions between the atoms, and in this liquidlike diffusion regime, dynamic asymmetry should be absent, as reflected in the Stokes-Einstein relation [see Eq. (1) below] [17]. In contrast, the dynamic asymmetry is very strong in the glassy state where the atoms have to overcome high activation barriers by local hopping, and diffusivities of the larger and smaller atoms can differ by many orders of magnitude. This has already been investigated intensively in binary Zr-based glasses such as *a*-Co-Zr and *a*-Ni-Zr [18–20]. Here, even different diffusion mechanisms were proposed for the larger Zr atoms and the smaller Co or Ni atoms. For the smaller atoms, a direct highly collective diffusion mechanism involving hopping of a large number of atoms was proposed based on the vanishing isotope effect [18] and pressure dependence [21], as well as on molecular dynamics simulations [22], where chainlike collective displacements were seen, for instance. In contrast, for the much larger Zr atoms, a pronounced activation volume of the order of an atomic volume was observed [20], suggesting a different mechanism based on the thermally activated opening of the nearest-neighbor cage which can be envisioned as being assisted by thermally generated smeared-out free volume.

A strong decoupling of the diffusivities of the larger Pd atoms and the smaller components was also seen in the supercooled liquid state of multicomponent Pd-based glass forming alloys below the critical temperature T_c of the mode coupling theory reaching 4 orders of magnitude at the caloric glass transition temperature T_g [7]. This was attributed to the freezing in of liquidlike diffusion at T_c–well above the caloric glass transition temperature—and the existence of a pronounced energy landscape and dynamic heterogeneities. Strong decoupling of the component diffusivities was also reported in Zr-based bulk glass forming alloys in the deeply supercooled liquid state [23–26]. In the equilibrium melt far above the liquidus temperature, however, the energy-landscape theory describes atoms as diffusing almost freely well above the peaks and valleys of the energy landscape, seeing only shallow minima [27]. In accord with this expectation, the diffusivities of all components of the above-mentioned Pd-based glass forming alloy were found to merge close to T_c. On the other hand, recent investigations on molecular glass formers indicate characteristics of glassy dynamics even above the melting temperature [28].

Here we report on radiotracer measurements of ^{95}Zr and ^{57}Co diffusion in the stable liquid state of a multicomponent bulk metallic glass forming $Zr_{46.75}Ti_{8.25}Cu_{7.5}Ni_{10}Be_{27.5}$ melt above the liquidus temperature. ^{57}Co is used as a convenient and well-established tracer for Ni diffusion [4,7]. The results are compared with viscosity data obtained by an elaborate containerless electrostatic levitation technique. While diffusion of the large Zr atoms obeys the Stokes-Einstein equation, a pronounced decoupling is observed between Zr diffusion and diffusion of the smaller Co atoms. This suggests that some signature of the aforementioned different diffusion mechanisms of the large Zr atoms and the smaller atoms observed in the glassy state, and, hence, strong influences of the energy landscape on diffusion, is still preserved even in the stable liquid state far above the liquidus temperature. The contrasting behavior with respect to the Pd-based glass forming alloy mentioned above will be discussed in terms of the sharply contrasting electronic properties of the very reactive Zr which has partially occupied d orbitals and can form directed bonds, and the noble metal palladium.

The $Zr_{46.75}Ti_{8.25}Cu_{7.5}Ni_{10}Be_{27.5}$ glass forming alloy (known as Vitreloy 4) was prepared and characterized as reported previously [29]. The caloric glass transition temperature T_g of 580 K (at 20 K/min) and the quasieutectic melting temperature T_m of 1050 K were determined by means of differential scanning calorimetry (DSC) at a heating rate of 20 K/min. Microscopic dynamics in the equilibrium liquid were studied by quasielastic neutron scattering (QNS) and were shown to be in accordance with the predictions of the mode coupling theory. The temperature dependence of the structural relaxation times as well as the temperature dependence of the amplitude and time scale of a localized cage motion (fast beta relaxation) extrapolate consistently to a T_c at 875 K [30]. For the diffusion measurements, the radiotracer technique in combination with serial sectioning and an elaborate encapsulation technique in a graphite container were employed. Radiotracer ^{57}Co was commercially available (Eckert & Ziegler, Braunschweig, Germany), and ^{95}Zr was obtained from neutron irradiation of enriched ^{94}Zr at Helmholtz Zentrum Berlin. Prior to the deposition of the tracers, cylindrical samples with 8 mm diameter and ~1 mm thickness were polished mirrorlike at one base. The deposition of ^{95}Zr was done electrochemically as described, e.g., in Ref. [20], and ^{57}Co was evaporated as described, e.g., in Ref. [7]. Because of the large penetration depth, serial sectioning was performed by mechanical grinding. Most of the diffusion measurements with ^{57}Co and ^{95}Zr were carried out separately in alloys from the same batch. Thus, possible errors due to slight variations in the alloy composition [31] were eliminated. To rule out effects of systematic errors, particularly in temperature, some ^{57}Co and ^{95}Zr diffusivities were also measured simultaneously (see Fig. 1 middle and Fig. 2). All the diffusion profiles are shown in Fig. 1. Tracer diffusivities were obtained via the thin film solution of Fick's second law from the slopes and the annealing times as described in Ref. [32]. Since the comparison of ^{57}Co and ^{95}Zr diffusion is crucial for the present work, surface hold-up effects caused by the bottom tracer layer on the diffusion of the top layer were ruled out via measurements with either ^{57}Co or ^{95}Zr as the top layer and otherwise identical conditions (see Fig. 2). These experiments also demonstrate the reproducibility of the diffusion measurements with error margins of the order of 20% for the same alloy.

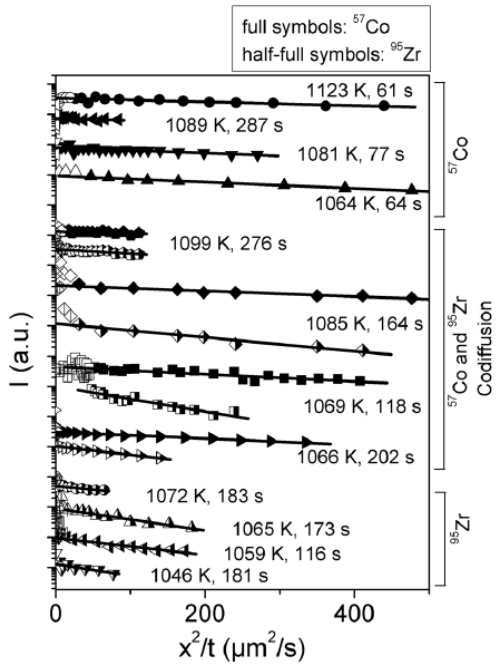

FIG. 1. ^{95}Zr and ^{57}Co penetration profiles. The activity of ^{95}Zr and ^{57}Co is plotted on a semilog scale vs the square of the penetration depth divided by the annealing time. Full and half-full symbols display ^{57}Co and ^{95}Zr diffusivities, respectively. Data points with open symbols close to the surface are affected by surface hold up and were not taken into account. Note that the profiles in the central part were obtained from simultaneous diffusion of both tracers to rule out systematic errors.

The viscosity measurements were performed in an electrostatic levitator using the oscillating drop technique [6,33]. The samples of 2–3 mm in diameter were levitated under high vacuum ($<1 \times 10^{-4}$ Pa) and molten with infrared lasers. The sample temperature was recorded with pyrometry. The excitation of the dipole oscillation was achieved by superimposing a small sinusoidal alternating electrical field onto the static levitation field. The frequency of the field was set to the eigenfrequency of the droplet. The damping of the oscillation, which was used to determine the viscosity, was recorded with a high-speed camera. Details are published elsewhere [34].

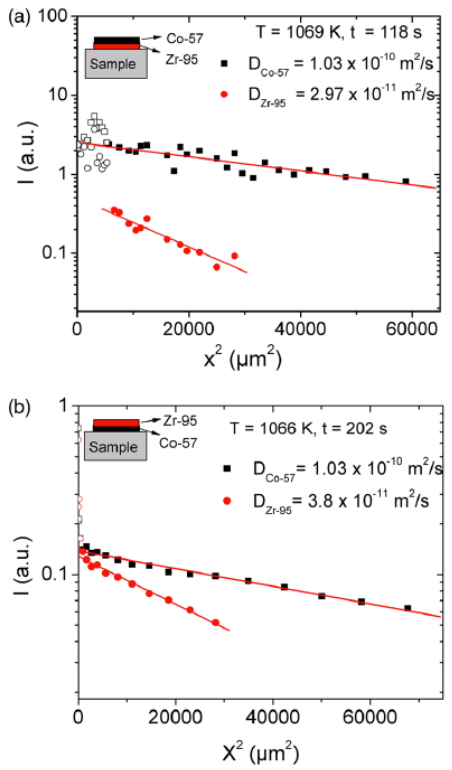

FIG. 2 (color online). ^{95}Zr and ^{57}Co penetration profiles from simultaneous diffusion of both tracers with different sequence of the tracer layers and otherwise identical conditions. (a) ^{57}Co layer on top of ^{95}Zr layer and (b) ^{95}Zr layer on top of ^{57}Co layer. Note the good agreement which allows hold-up effects caused by the bottom layer on diffusion of the top layer to be excluded.

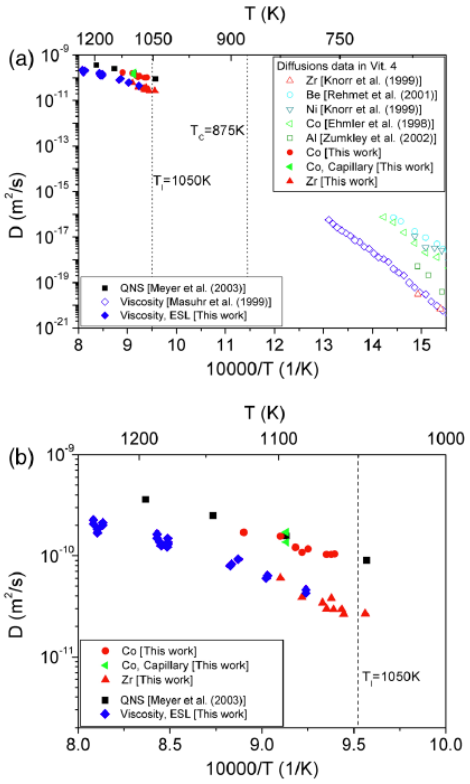

FIG. 3 (color online). (a) Arrhenius plot of diffusion in $Zr_{46,75}Ti_{8,25}Cu_{7,5}Ni_{10}Be_{27,5}$ (Vitreloy 4) in the stable and in the supercooled liquid state. The present ^{95}Zr and ^{57}Co diffusivities, including data points obtained with the long capillary technique (green triangles), are shown together with diffusivities from QNS [29] and tracer diffusivities from the literature (Knorr *et al.* [23], Rehmet *et al.* [24], Ehmler *et al.* [25], and Zumkley *et al.* [26]). The QNS data essentially represent diffusivities of Cu and Ni [29,30]. Also shown are diffusivities converted via the Stokes-Einstein equation from the present viscosity data measured using electrostatic levitation. The radius of 145 pm was taken, which represents Zr atoms; however, taking radii of the smaller components would not lead to any significant changes on the present log scale. Dashed lines mark the quasieutectic melting temperature T_m and the critical temperature T_c of the mode coupling theory determined form quasielastic neutron scattering. The caloric glass transition temperature T_g (not shown) is 580 K (from DSC at 20 K/ min). (b) Magnified view of (a) showing only the range of the stable liquid state.

Figure 3(a) shows the ^{95}Zr and ^{57}Co diffusivities reported here, together with radiotracer diffusivities of various elements taken from the literature. A magnified view of the most interesting range in the stable liquid state is displayed in Fig. 3(b). These figures also depict the results from quasielastic neutron scattering mentioned above, which essentially represent diffusivities of Cu and Ni (and, hence, of ^{57}Co taken here as a tracer for Ni), because of the small coherent neutron cross section of Zr, as also confirmed earlier by comparison with radiotracer experiments [7,29]. The good agreement seen in Fig. 3 between the diffusivities from the QNS and the present ^{57}Co diffusivities has to be pointed out because the QNS measurements are not affected by convection [7,26], which often severely influences diffusion measurements in ordinary liquids and melts under gravity. Thus, convection effects on the present measurements can be ruled out even in the stable liquid state investigated here. This can be attributed to the high viscosity of bulk glass forming alloys [7]. The absence of convection was also corroborated through comparison with radiotracer experiments, which we performed by means of the long capillary technique. This technique is a well-known method to minimize convection [35]. The resulting diffusivities are included in Fig. 3. and are in excellent agreement with the other data. Details will be reported elsewhere.

The striking observation in Figs. 3(a) and 3(b) is the decoupling of Zr diffusion from the diffusion of the smaller components in the stable liquid state reaching a factor as large as 4 at the liquidus temperature. The decoupling decreases at higher temperatures, and extrapolation of the

data in Fig. 3 suggests a value smaller than a factor of 2 above 1250 K. This is in line with the previous QNS results [36] showing that at 1255 K, the measured density correlation function decays completely to zero on a time scale of about 20 ps and does not exhibit a very strong stretching behavior. On the other hand, the QNS experiment could not reveal a slow Zr dynamics at the liquidus temperature, which exceeds the experimental time window.

We point out that one has to discriminate between the observed decoupling of the diffusion of different species, here referred to as component decoupling in contrast to viscous decoupling between viscosity and the diffusivities. The viscous decoupling could be regarded as just a consequence of the effect of the broadening of the distribution of mobilities and the different ways transport and relaxation sample that distribution; i.e., viscous decoupling (because it involves two qualitatively different physical quantities) may be considered as reflecting something rather general about the statistics of dynamics. In contrast, the component decoupling must have an explicit structural origin and reveals information on the relation between composition and atomic dynamics.

As mentioned earlier, component decoupling is not expected in stable liquids exhibiting ordinary liquidlike diffusion governed by uncorrelated binary atomic collisions. A commonly used relation which connects diffusivity and liquid viscosity is the Stokes-Einstein (SE) equation,

$$D = \frac{k_B T}{6\pi\eta r}, \tag{1}$$

according to which diffusivities should scale with $1/r$, and, hence, the diffusivities of all components should essentially be equal. In Eq. (1), D is the diffusion coefficient, η is the viscosity, k_B the Boltzmann constant, and r the particle radius. The decoupling of Zr diffusion from diffusion of the small components is even more striking in view of the fact that the SE equation is well obeyed for Zr diffusion. This is also shown in Figs. 3(a) and 3(b) where the viscosity data obtained from the present electrostatic levitation measurements based on the oscillating drop technique (see above) were converted into diffusivities via the SE equation. Together with the converted viscosity data of Masuhr *et al.* [37] and the Zr diffusion data of Knorr *et al.* [23] close to the caloric glass transition temperature, Fig. 3 suggests the SE equation to hold in the whole temperature range from the stable equilibrium melt down to T_g encompassing more than 10 orders of magnitude. The validity to the SE equation for the large alloy component was also reported earlier for Pd in Pd-based glass formers and was interpreted in terms of the existence of a slow subsystem made up by the large atoms that has to rearrange for structural relaxation and viscous flow [7]. The formation of the slow subsystem was attributed to the interplay of size disparity and chemical short-range order.

Within this notion, the present investigations show that the decoupling of diffusion of the small components from the slow Zr subsystem is still preserved in the stable liquid state at least 150 K above the liquidus temperature and, as suggested by an extrapolation of the data in Figs. 3(a) and 3(b), even at much higher temperatures. Apparently, the diffusion of the large Zr atoms is still strongly affected by the energy landscape more than 300 K above T_c, where liquidlike diffusion is expected to freeze in [38]. This suggests that the gradual decay of the diffusion barriers, which was observed to set in at T_c [7], extends over several hundred K in the present multicomponent metallic glass forming alloy. Consequently, Zr and the small components still seem to diffuse via different mechanisms in the stable liquid state well above T_l. This lends support to the model of local configurational excitations in the atomic connectivity network recently proposed by Egami and co-workers based on molecular dynamics simulations on metallic melts, including Zr based alloys [39]. In these terms, Zr atoms in the melt form significantly stronger temporary nearest-neighbor bonds that have to be broken by thermal activation compared to the other atoms. The Egami model is also nicely confirmed by comparing the present data with those obtained in the Pd-based glass forming melt discussed above [7]. The very reactive Zr has partially occupied d orbitals and can form directed bonds, whereas the noble metal Pd is expected to form much weaker nondirected bonds. Hence, Zr atoms in the melt should form significantly stronger temporary nearest-neighbor bonds that have to be broken by thermal activation compared to Pd. This explains why for the Pd-based glass forming melt, the influence of the energy landscape is much smaller.

In conclusion, the present results show that both diffusion and viscous flow start to develop solidlike, i.e., energy-landscape-controlled, features upon cooling far above the liquidus temperature and many hundred K above the mode coupling T_c in the multicomponent glass forming alloy investigated here.

The authors would like to thank Thomas Voigtmann (DLR Köln) and Takeshi Egami (University of Tennessee) for fruitful discussions. Financial support by German Research Foundation (Deutsche Forschungsgemeinschaft) under the Projects No. Fa 234/22-1, No. Ra 796/4, and No. Me 1958/10-1 is gratefully acknowledged. We would also like to thank Gregor Bukalis from Helmholtz Zentrum Berlin for irradiation of the Zr tracers.

*ff@tf.uni-kiel.de

[1] J. Schroers, Phys. Today **66**, No. 2, 32 (2013).
[2] A. Inoue and N. Nishiyama, MRS Bull. **32**, 651 (2007).
[3] B. Zberg, P. J. Uggowitzer, and J. F. Löffler, Nat. Mater. **8**, 887 (2009).

[4] F. Faupel, W. Frank, M.-P. Macht, H. Mehrer, V. Naundorf, K. Rätzke, H. R. Schober, S. K. Sharma, and H. Teichler, Rev. Mod. Phys. **75**, 237 (2003).
[5] H. B. Yu, K. Samwer, Y. Wu, and W. H. Wang, Phys. Rev. Lett. **109**, 095508 (2012).
[6] J. Brillo, A. I. Pommrich, and A. Meyer, Phys. Rev. Lett. **107**, 165902 (2011).
[7] A. Bartsch, K. Rätzke, A. Meyer, and F. Faupel, Phys. Rev. Lett. **104**, 195901 (2010).
[8] S. Wei, F. Yang, J. Bednarcik, I. Kuban, O. Shuleshova, A. Meyer, and R. Busch, Nat. Commun. **4**, 2083 (2013).
[9] H. Tanaka, J. Phys. Condens. Matter **12**, R207 (2000).
[10] T. Voigtmann and J. Horbach, Phys. Rev. Lett. **103**, 205901 (2009).
[11] M. D. Ediger and P. Harrowell, J. Chem. Phys. **137**, 080901 (2012).
[12] Z. Evenson and R. Busch, Acta Mater. **59**, 4404 (2011).
[13] Z. Evenson and R. Busch, J. Alloys Compd. **509**, S38 (2011).
[14] R. Busch, J. Schroers, and W. H. Wang, MRS Bull. **32**, 620 (2007).
[15] A. L. Greer, Nature (London) **366**, 303 (1993).
[16] A. L. Greer, Science **267**, 1947 (1995).
[17] J. S. Kirkaldy and D. J. Young, *Diffusion in the Condensed State* (The Institute of Metals, London, 1987).
[18] A. Heesemann, V. Zöllmer, K. Rätzke, and F. Faupel, Phys. Rev. Lett. **84**, 1467 (2000).
[19] U. K. Rossler and H. Teichler, Phys. Rev. E **61**, 394 (2000).
[20] P. Klugkist, K. Rätzke, and F. Faupel, Phys. Rev. Lett. **81**, 614 (1998).
[21] P. Klugkist, K. Rätzke, S. Rehders, P. Troche, and F. Faupel, Phys. Rev. Lett. **80**, 3288 (1998).
[22] D. Caprion, J. Matsui, and H. R. Schober, Phys. Rev. Lett. **85**, 4293 (2000).
[23] K. Knorr, M. P. Macht, and H. Mehrer, Mater. Res. Soc. Symp. Proc. **554**, 269 (1999).
[24] A. Rehmet, K. Rätzke, F. Faupel, P. D. Eversheim, K. Freitag, U. Geyer, and S. Schneider, Appl. Phys. Lett. **79**, 2892 (2001).
[25] H. Ehmler, A. Heesemann, K. Rätzke, F. Faupel, and U. Geyer, Phys. Rev. Lett. **80**, 4919 (1998).
[26] T. Zumkley, V. Naundorf, M.-P. Macht, P. Fielitz, and G. Frohberg, Mater. Trans., JIM **43**, 1921 (2002).
[27] P. Debenedetti and F. H. Stillinger, Nature (London) **410**, 259 (2001).
[28] N. Petzold, B. Schmidtke, R. Kahlau, D. Bock, R. Meier, B. Micko, D. Kruk, and E. A. Rössler, J. Chem. Phys. **138**, 12A510 (2013).
[29] A. Meyer, W. Petry, M. Koza, and M.-P. Macht, Appl. Phys. Lett. **83**, 3894 (2003).
[30] A. Meyer, J. Wuttke, W. Petry, O. G. Randl, and H. Schober, Phys. Rev. Lett. **80**, 4454 (1998).
[31] G. Kumar, P. Staffer, J. Blawzdziewicz, U. Schwarz, and J. Schroers, Appl. Phys. Lett. **97**, 101907 (2010).
[32] A. Bartsch, K. Rätzke, F. Faupel, and A. Meyer, Appl. Phys. Lett. **89**, 121917 (2006).
[33] I. Egry, H. Giffard, and S. Schneider, Meas. Sci. Technol. **16**, 426 (2005).
[34] F. Yang, T. Unruh, and A. Meyer Europhys. Lett. **107**, 26001 (2014).
[35] H. Müller and G. Müller-Vogt, Cryst. Res. Technol. **38**, 707 (2003).
[36] F. Yang, T. Kordel, D. Holland-Moritz, T. Unruh, and A. Meyer, J. Phys. Condens. Matter **23**, 254207 (2011).
[37] A. Masuhr, T. A. Waniuk, R. Busch, and W. L. Johnson, Phys. Rev. Lett. **82**, 2290 (1999).
[38] W. Götze, J. Phys. Condens. Matter **11**, A1 (1999).
[39] T. Iwashita, D. M. Nicholson, and T. Egami, Phys. Rev. Lett. **110**, 205504 (2013).

Appendix B Details of the experimental results

A. ^{57}Co and ^{95}Zr diffusivities data of $Zr_{46.75}Ti_{8.25}Cu_{7.5}Ni_{10}Be_{27.5}$ melt‡

^{57}Co diffusivities data from the individual measurement

$T\ (K)$	$t\ (s)$	$D\ (m^2/s)$	$2\sqrt{Dt}$ (μm)
1089	287	1.21 x 10^{-10}	372.7
1123	61	1.70 x 10^{-10}	203.7
1081	77	1.17 x 10^{-10}	190.1
1064	64	1.04 x 10^{-10}	163.2

^{95}Zr diffusivities data from the individual measurement

$T\ (K)$	$t\ (s)$	$D\ (m^2/s)$	$2\sqrt{Dt}$ (μm)
1072	183	3.43 x 10^{-11}	158.4
1065	172	2.95 x 10^{-11}	142.7
1046	181	2.68 x 10^{-11}	139.3
1059	116	2.66 x 10^{-11}	111.1

^{57}Co and ^{95}Zr diffusivities data from the simultaneous measurement

$T\ (K)$	$t\ (s)$	^{57}Co		^{95}Zr	
		$D\ (m^2/s)$	$2\sqrt{Dt}$ (μm)	$D\ (m^2/s)$	$2\sqrt{Dt}$ (μm)
1099	276	1.56 x 10^{-10}	415.0	6.04 x 10^{-11}	258.2
1085	164	1.08 x 10^{-10}	265.9	3.89 x 10^{-11}	159.5
1069	118	1.03 x 10^{-10}	220.5	2.97 x 10^{-11}	118.4

‡ The correction factor as mentioned in section 3.7 is 1.03, which is only 3 % higher than the measured diffusivities. As it is still within the experimental error bar, it is not included in the calculation of diffusivities shown in this table.

^{57}Co diffusivities data from the measurement using long capillary technique

$T\ (K)$	$t\ (s)$	$D\ (m^2/s)$	$2\sqrt{Dt}$ (μm)
1095	965	1.36 x 10^{-10}	724.4
1095	1002	1.71 x 10^{-10}	827.9

B. ^{57}Co and ^{95}Zr diffusivities data from the simultaneous measurement on $Zr_{64}Ni_{36}$ melt

$T\ (K)$	$t\ (s)$	**f**	^{57}Co		^{95}Zr	
			$D\ (m^2/s)$	$2\sqrt{Dt}$ (mm)	$D\ (m^2/s)$	$2\sqrt{Dt}$ (mm)
1304	414	1.01	8.15 x 10^{-10}	1.16	5.62 x 10^{-10}	0.96
1388	677	1.98	1.07 x 10^{-9}	1.70	1.19 x 10^{-9}	1.79
1388	677	1.98	1.29 x 10^{-9}	1.87	1.30 x 10^{-9}	1.87
1438	685	1.22	1.36 x 10^{-9}	1.93	1.13 x 10^{-9}	1.76
1438	932	1.23	1.41 x 10^{-9}	2.30	1.38 x 10^{-9}	2.27

C. ^{57}Co and ^{95}Zr diffusivities data from the simultaneous measurement on $Zr_{60}Ni_{25}Al_{15}$ melt

$T\ (K)$	$t\ (s)$	**f**	^{57}Co		^{95}Zr	
			$D\ (m^2/s)$	$2\sqrt{Dt}$ (mm)	$D\ (m^2/s)$	$2\sqrt{Dt}$ (mm)
1290	542	1.11	4.38 x 10^{-10}	0.97	3.71 x 10^{-10}	0.90
1388	686	1.37	7.46 x 10^{-10}	1.43	5.75 x 10^{-10}	1.26

D. ^{57}Co and ^{95}Zr diffusivities data from the simultaneous measurement on $Zr_{36}Ni_{64}$ melt

$T\ (K)$	$t\ (s)$	**f**	^{57}Co		^{95}Zr	
			$D\ (m^2/s)$	$2\sqrt{Dt}$ (mm)	$D\ (m^2/s)$	$2\sqrt{Dt}$ (mm)
1388	1038	1.01	5.51 x 10^{-10}	1.51	4.32 x 10^{-10}	1.34
1388	655	1.01	6.10 x 10^{-10}	1.26	4.42 x 10^{-10}	1.08
1428	661	1.03	7.25 x 10^{-10}	1.38	5.20 x 10^{-10}	1.17
1469	596	1.66	9.70 x 10^{-10}	1.52	6.91 x 10^{-10}	1.28
1469	596	1.66	8.92 x 10^{-10}	1.46	7.14 x 10^{-10}	1.31
1488	763	1.09	1.02 x 10^{-9}	1.76	7.16 x 10^{-10}	1.48

Erklärung

Hiermit erkläre ich, dass die beigefügte Dissertation, abgesehen von der Beratung durch den Betreuer, nach Inhalt und Form meine eigene Arbeit ist.

Die Arbeit, ganz oder zum Teil, wurde nie schon einer anderen Stelle im Rahmen eines Prüfungsverfahrens vorgelegt, und ist nie veröffentlicht worden oder zur Veröffentlichung eingereicht worden.

Außerdem ist die Arbeit unter Einhaltung der Regeln guter wissenschaftlicher Praxis der Deutschen Forschungsgemeinschaft entstanden.

Kiel, den 02.02.2015 _____

Sri Wahyuni Basuki